







Cite this: *Phys. Chem. Chem. Phys.*,
2021, 23, 25612

Ultrafast relaxation investigated by photoelectron circular dichroism: an isomeric comparison of camphor and fenchone

Valérie Blanchet, , Dominique Descamps, , Stéphane Petit, Yann Mairesse, 
Bernard Pons and Baptiste Fabre *

We study the isomeric effects using time resolved photoelectron circular dichroism (TR-PECD). Using a (1 + 1') pump–probe ionisation scheme with photoelectrons collected by the velocity map imaging technique, we compare the relaxation dynamics from the 3s-Rydberg state in 1*R*,4*R*-(+)-camphor with the one in its chiral isomer, 1*R*,4*S*-(–)-fenchone [Comby *et al.*, 2016, *JPCL*, **7**, 4514]. Our measurements revealed a similar lifetime for both isomers. However, the circular dichroism in the photoelectron angular distribution decays exponentially in ~730 fs from a +9% forward amplitude during the first hundreds of femtoseconds to reach an asymptotic –2% backward amplitude. This time-scale is drastically shorter than in fenchone. Our analysis allows us to evaluate the impact of the anisotropy of excitation; the relaxation dynamics, following photoexcitation by the linearly polarized pump, is then compared to that induced by a circularly polarized pump pulse (CPL). With such a CPL pump, we then retrieve time constants of our chiral observables similar to the ones recorded in fenchone. Quantum and classical simulations are developed and used to decipher the dependence of the PECD on the anisotropy of excitation and the spatial distribution of the 3s-Rydberg electron wavefunction. Our experimental investigations, supported by our simulations, suggest that varying the pump ellipticity enables us to reveal the breakdown of the Franck–Condon approximation.

Received 3rd August 2021,
Accepted 19th October 2021

DOI: 10.1039/d1cp03569j

rsc.li/pccp

1 Introduction

Photoionization of randomly oriented chiral molecules by circularly polarized photons leads to an asymmetric photoelectron momentum distribution with respect to the light propagation direction.^{1–4} This forward/backward asymmetry, known as PhotoElectron Circular Dichroism (PECD), has mainly been studied in the Vacuum UltraViolet (VUV) spectral range where ionization results from the absorption of a single photon with energy larger than the Ionization Energy (IE) of the molecule. The PECD reverses sign as the circularly polarized light changes from left (LCP) to right (RCP) in a given enantiomer, or equivalently, when the molecular handedness is flipped for a fixed light helicity. In this single-photon ionization regime, the PECD results from the scattering of the outgoing electron onto the chiral potential. This asymmetric scattering induces chiro-sensitivity of the ionization time delays which differ by a few tens of attoseconds depending on the emission angle.⁵ PECD depends on the orbital from which the electron is pulled out as well as on the kinetic energy of the emitted photoelectron.⁶ Importantly,

PECD is remarkably sensitive to the molecular structure, being able to distinguish isomers,⁷ conformers,^{8,9} chemical substitution,¹⁰ clustering¹¹ and vibrational excitation.^{12,13} VUV-PECD has been extended to the Resonance-Enhanced MultiPhoton Ionization regime (REMPI), using ultraviolet femtosecond^{14,15} or nanosecond¹⁶ laser pulses. The resonant intermediate state(s) may strongly influence the forward/backward asymmetry. Last, PECD has been shown to persist in the strong-field regime¹⁷ where ionization proceeds in terms of tunneling through the ionic potential barrier lowered by the laser field. In that case, the asymmetry is encoded in the photoelectron distribution not only during the scattering of the freed electron onto the chiral potential but also during the primary tunneling process.¹⁸ PECD is thus a universal feature of the ionization of chiral molecules, occurring in all ionization regimes.¹⁷ Besides its fundamental importance, PECD can also be employed as a quantitative probe of chemical and enantiomeric composition of gas phase chiral mixtures.^{19–22} The high structural sensitivity of PECD imaging makes it a promising spectroscopic observable to track time-resolved dynamics induced in chiral molecular systems.

In Time-Resolved PECD (TR-PECD), a pump pulse launches a wavepacket in electronic state(s) and the ensuing relaxation dynamics are probed *via* photoionisation by monitoring the

Université de Bordeaux-CNRS-CEA, CELIA, UMR5107, F33405 Talence, France.
E-mail: baptiste.fabre@u-bordeaux.fr

time-dependencies of the PECD. In this respect, TR-PECD is an extension of REMPI-PECD to the temporal domain. In the pioneering TR-PECD experiment,²³ we studied the relaxation dynamics taking place from the 3s-Rydberg state in fenchone ($C_{10}H_{16}O$).^{23,24} The temporal features in the PECD observables were then associated to internal vibrational redistribution that remained hidden in the angle-integrated photoelectron spectrum-TR-PES (Time-Resolved PhotoElectron Spectrum). This first investigation established TR-PECD as a new and unparalleled observable of relaxation dynamics in excited chiral systems. In the present paper, we extend this previous work to camphor molecules. Camphor is an isomer of fenchone which only differs by the location of two methyl groups, as shown in Fig. 1(a) and (b). As in the fenchone experiment,²³ camphor is photoexcited into its 3s-Rydberg state with a UV pump pulse before being ionized by a delayed and circularly polarized probe pulse in order to investigate the temporal evolution of PECD. The main objective of this pump-probe experiment is to observe the sensitivity of PECD to relaxation dynamics and to isomerism.

In the following, we are concerned with an ionization taking place around 9.2 eV, near the ionization energy of camphor ($IE = 8.66 \pm 0.01$ eV²⁵). PECD in static camphor has been studied in the VUV spectral range.^{7,10} At 9.2 eV, the VUV-PECD of 1*R*,4*R*(+)-camphor ionized by left-polarized light (LCP) has $\sim -5\%$ amplitude – the electrons are preferentially emitted in the backward hemisphere. Following the same Cahn-Ingold-Prelog sequence for the first chiral center (in C1), the closest rigid isomer of 1*R*,4*R*(+)-camphor is 1*R*,4*S*(–)-fenchone. The VUV-PECD of the latter reaches $\sim +15\%$ at 9.2 eV.⁷ There is thus a huge isomerism effect in one-photon ionization of fenchone and camphor near the ionization threshold. These two isomers however have very similar Highest Occupied Molecular Orbitals (HOMO, see Fig. 1(c) and (d)) from which the electron is pulled out. Therefore, this isomerism effect recorded in the VUV range stems from different electron scatterings in fenchone and camphor, leading to different final projections of the electron in the molecular continuum. PECD in static camphor has also been observed in a (2 + 1)-REMPI scheme where the two first photons reach the 3s-Rydberg state and one additional photon ionizes the molecule.^{15,26} The (2 + 1)-REMPI-PECD of 1*R*,4*R*(+)-camphor reverses sign with respect to its VUV counterpart, presenting a $\sim +8\%$ amplitude. Such a behaviour is understood as the influence of the intermediate 3s resonance. Conversely, the (2 + 1)-REMPI-PECD of 1*R*,4*S*(–)-fenchone reaches similar values as its VUV counterpart, with an amplitude of $\sim +12\%$.^{24,26} This comparison raises the question of the role of the intermediate 3s resonance in the PECD, which the present work aims at re-examining in a time-resolved (1 + 1')-REMPI scheme.

Here, camphor molecules will be promoted to their excited 3s state through the absorption of one pump photon before being ionized by one delayed probe photon of distinct energy. The relaxation dynamics of the 3s-Rydberg state will be observed through the temporal dependence of both the symmetric and asymmetric parts of the photoelectron momentum distribution. Comparison with our previous experiments in fenchone²³ will enable us to reveal the sensitivity of relaxation dynamics to

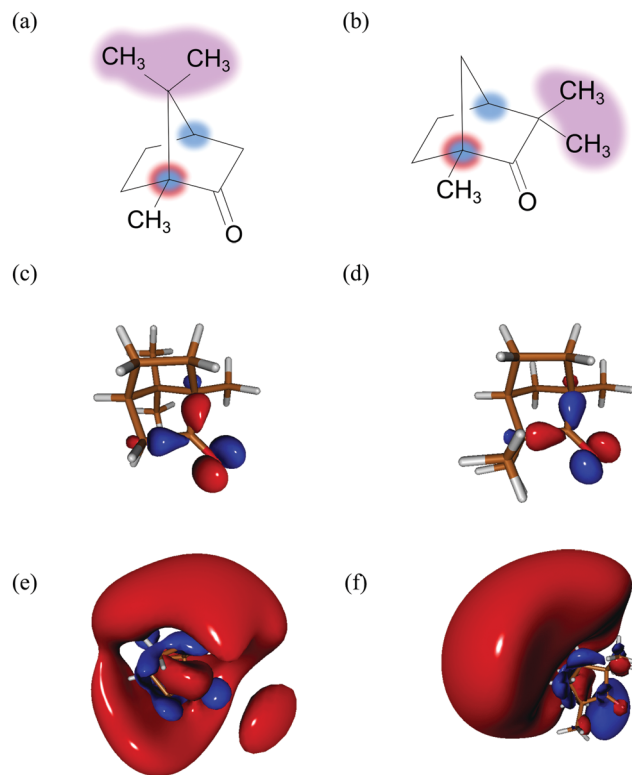


Fig. 1 Two monoterpenoid isomers – the most abundant enantiomers in nature: (a) 1*R*,4*R*(+)-camphor and (b) 1*R*,4*S*(–)-fenchone with the 1*R* chiral carbon labelled in blue/red and 4*R*/4*S* in blue. Similarities between the HOMO orbital of camphor (c) and fenchone (d). The orbital 3s of camphor (e) and fenchone (f) populated by the pump pulse.

isomerism, even if fenchone and camphor are *a priori* excited to a similar 3s-Rydberg state (see Fig. 1(e) and (f)) with similar anisotropy of excitation and subject also to vibronic relaxations. This will adequately complement the previous static studies.

The paper is structured as follows. In Section 2, we describe the experimental setup based on a Velocity-Map Imaging (VMI) spectrometer and each step involved in extracting TR-PECD from raw VMI-images. In Section 3, we present and discuss the ion and PECD transients for three different polarizations of the pump ($S_3 = \pm 1, 0$), in line with the recent work on limonene²⁷ in which we investigated the influence of the anisotropy of excitation. In Section 4, we introduce the theoretical background used to model the photoelectron angular spectrum and associated PECD in the static (1 + 1')-REMPI regime. Special attention is paid to the origin of isomerism effects in this interaction scheme by comparing the TR-PECD recorded on 1*R*,4*R*(+)-camphor with the one obtained in 1*R*,4*S*(–)-fenchone. This section also includes a theoretical investigation on how the decay of the anisotropy of excitation impacts the TR-PECD. Finally, we summarize our findings in Section 5.

2 Experimental description

2.1 Experimental setup

The experimental setup consists of a molecular beam chamber with a 1 kHz Even-Lavie pulsed valve, coupled to a velocity-map

imaging (VMI) spectrometer and a 26 fs–1 kHz-Ti:sapphire laser system (Aurore facility²⁸ – 800 nm). The enantiomerically pure sample of 1R,4R-(+)-camphor has been provided by Sigma-Aldrich with 98% chemical purity and an optical rotation quoted at $\alpha_D^{25} = 44.1^\circ$. The pulsed valve, with a 250 μm conical nozzle, is used at 80 $^\circ\text{C}$ to get a significant vapour pressure and to avoid cluster formation with the minimal 8 bars of helium required to get a stable pulsed molecular beam. Typically this seeded supersonic molecular beam ($\sim 1000 \text{ km s}^{-1}$) generates a rotational temperature on camphor of few tens of kelvin.^{29,30}

One part of the laser beam is used to generate the pump pulse at 6.16 eV (201.3 nm) with a 25 meV Full Width Half Maximum (FWHM). With these UV pulse characteristics, the 3s-Rydberg state of camphor is expected to be vibrationally excited with less than 100 meV.³¹ To photoionize near 9.2 eV, the probe pulse is simply the second harmonic of the fundamental pulse centered at 3.1 eV ($\lambda = 400 \text{ nm}$) with a 100 meV bandwidth. The $(1 + 1')$ total energy is 600 meV above the IE and 440 meV below the dissociative ionization threshold.⁷ This excitation scheme is summarized in Fig. 2. The pump and probe beams are focused on the molecular beam with $f = 250 \text{ mm}$ and $f = 600 \text{ mm}$ focal lenses, respectively, and crossed with a 4° angle. In order to restrain the excitation scheme to $(1 + 1')$, the pump ($3 \mu\text{J p}^{-1}$) and probe ($8 \mu\text{J p}^{-1}$) intensities are maintained quite low at 5×10^{11} and $1 \times 10^{11} \text{ W cm}^{-2}$, respectively. This soft ionization produces only 9% of dissociative ionization events *via* a $(1 + 1' + 1')$ -scheme. The circular polarizations have been obtained by introducing a zeroth order quarter waveplate on the probe beam and a Berek compensator adjusted to a $\pi/4$ phase delay on the pump beam. The cross-correlation time as well as the time overlap has not been determined on another molecular compound but extracted from the fit of the transients of the parent ion ($\text{C}_{10}\text{H}_{16}\text{O}^+$). The cross-correlation time is $\sim 200 \text{ fs}$ due to the residual chirp of the UV pump pulse.

The photoelectrons have been collected in a direction perpendicular to the plane defined by the laser and molecular beams, and detected at the end of a 40 cm time-of-flight tube using an imaging detector consisting of two micro-channel

plates (MCP – 7 cm in diameter) coupled to a phosphor screen (P43) and a 16 bit CCD camera. An energy resolution of 82 meV for photoelectrons at 0.7 eV kinetic energy was determined by photoionizing krypton atoms. The optimisation of $\pm 45^\circ$ angles relative to the neutral axis of the quarter waveplate of the probe was first done optically with a polarizer, and an accuracy better than one degree was achieved *via* the optimization of the one-colour PECD images recorded at 400 nm.¹⁴ This results in an electron yield of the $1 + (1'\text{-RCP})$ ionization 0.6% higher than the one associated to $1 + (1'\text{-LCP})$. This difference that stems from the quarter waveplate limitations was corrected by multiplying each pixel of the images recorded with a left-circularly polarized probe by a factor of 1.006.

Ionization data were recorded by scanning the pump–probe delays typically twenty times: for each probe helicity and at each delay, one pump–probe image was recorded over 51 000 laser shots. For each scan and due to the commensurability between $(1 + 1')$ and $(2' + 1')$ ionization, two background images corresponding to the probe pulse alone at each helicity were recorded and subtracted from each pump–probe image.

2.2 Data processing

For a given pump–probe delay t , the VMI spectrometer provides 2D photoelectron angular distributions $P_{S_3, \pm 1}(E_{\text{kin}}, \theta', t)$ in which the third Stokes parameter S_3 defines the amount of circularly polarized photons of the pump pulse, whereas the polarisation state of the probe is equal to ± 1 (RCP/LCP). E_{kin} is the kinetic energy of the photoelectron and θ' is the polar angle in the VMI detector plane. $\theta' = 0$ points to the (forward) direction of light propagation while $\theta' = 180^\circ$ points backward. The VMI images are projections of the 3D differential ionization cross sections $\mathcal{P}_{S_3, \pm 1}(E_{\text{kin}}, \theta, \varphi, t)$, where θ and φ are the spherical angles defining the direction of photoelectron ejection. This cross section, resulting from two-photon absorption, can be decomposed as

$$\mathcal{P}_{S_3, \pm 1}(E_{\text{kin}}, \theta, \varphi, t) = \sum_{\ell=0}^4 \sum_{\substack{m=-1 \\ |2m| \leq \ell}}^1 \mathcal{B}_{\ell, 2m}^{S_3, \pm 1}(E_{\text{kin}}, t) Y_{\ell}^{2m}(\theta, \varphi) \quad (1)$$

where $\mathcal{Y}_{\ell}^{2m}(\theta, \varphi)$ are cosine ($m > 0$) and sine ($m < 0$) real spherical harmonics. It can be shown analytically, as in ref 32 and 33, that the asymmetric part of the electron yield is directly related to the coefficients $\mathcal{B}_{\ell, 2m}^{S_3, \pm 1}(E_{\text{kin}}, t)$ with either (ℓ odd and $m \geq 0$) or (ℓ even and $m < 0$), while the symmetric part depends on the remaining ones. The coefficient $\mathcal{B}_{0,0}^{S_3, \pm 1}(E_{\text{kin}}, t)$ is the TR-PES. We detail in the following the procedure which is implemented to link the 2D $P_{S_3, \pm 1}(E_{\text{kin}}, \theta', t)$ and the 3D $\mathcal{P}_{S_3, \pm 1}(E_{\text{kin}}, \theta, \varphi, t)$ distributions, depending on the polarization state of the pump which can be linear ($S_3 = 0$) or circular ($S_3 = \pm 1$).

2.2.1 TR-PECD with a circularly polarized pump. When the pump beam is circularly polarized ($S_3 = \pm 1$), the differential cross section has a cylindrical symmetry about the light propagation axis. The decomposition (1) is then restricted

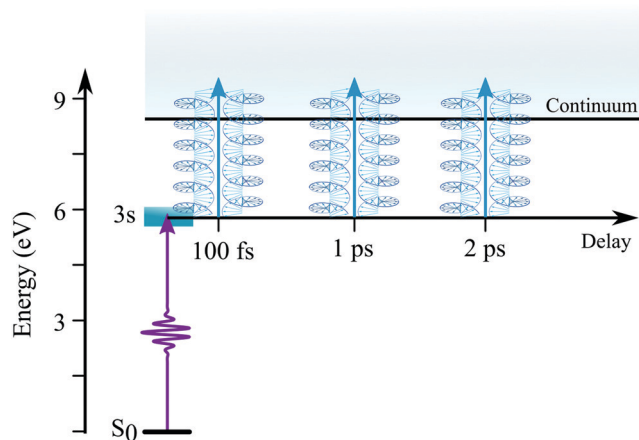


Fig. 2 Schematic of the excitation scheme used to measure TR-PECD from the 3s-Rydberg state of camphor.

to $2m = 0$, and its projection onto the VMI detector plane directly yields³⁴

$$P_{\pm 1, \pm 1}(E_{\text{kin}}, \theta', t) = \sum_{\ell=0}^4 B_{\ell}^{\pm 1, \pm 1}(E_{\text{kin}}, t) P_{\ell}(\cos \theta') \quad (2)$$

where $P_{\ell}(\cos \theta')$ are projections of Legendre polynomials onto the VMI plane. The parameters $B_{\ell}^{\pm 1, \pm 1}(E_{\text{kin}}, t)$ with odd ℓ reverse sign as the probe helicity changes from +1 to −1, or equivalently, as the enantiomeric nature of the sample changes from (+) to (−) for a fixed helicity. The even parameters are independent of both the probe helicity and the enantiomer. Furthermore, the values of all $B_{\ell}^{\pm 1, \pm 1}(E_{\text{kin}}, t)$ coefficients do not depend on the pump helicity. Therefore, we use the following convention: $B_{\ell}(E_{\text{kin}}, t) \equiv B_{\ell}^{\pm 1, \pm 1}(E_{\text{kin}}, t)$, keeping in mind that $B_{\ell}^{\pm 1, +1}(E_{\text{kin}}, t) = (-1)^{\ell} B_{\ell}^{\pm 1, -1}(E_{\text{kin}}, t)$. The B_{ℓ} parameters are related to those entering the definition (1) of the differential cross section by $B_{\ell} = \sqrt{2\ell + 1} B_{\ell, 2m=0}^{\pm 1, -1}$ because of the relationship between $2m = 0$ spherical harmonics and Legendre polynomial projections.

The forward/backward symmetric part of (2), $S^{\pm 1}(E_{\text{kin}}, \theta', t)$, is obtained by averaging the VMI signals associated to left-handed and right-handed probe polarizations:

$$S^{\pm 1}(E_{\text{kin}}, \theta', t) = \frac{P_{\pm 1, -1}(E_{\text{kin}}, \theta', t) + P_{\pm 1, +1}(E_{\text{kin}}, \theta', t)}{2}, \quad (3)$$

which gives, according to (2),

$$S^{\pm 1}(E_{\text{kin}}, \theta', t) = B_0(E_{\text{kin}}, t) P_0(\cos \theta') + B_2(E_{\text{kin}}, t) P_2(\cos \theta') + B_4(E_{\text{kin}}, t) P_4(\cos \theta'). \quad (4)$$

In order to avoid experimental artifacts, the $S^{\pm 1}(E_{\text{kin}}, \theta', t)$ images are numerically up/down and forward/backward symmetrized, as illustrated in Fig. 3(a).

The antisymmetric chiro-sensitive part of the 2D VMI distribution, $A^{\pm 1}(E_{\text{kin}}, \theta', t)$, is obtained by subtracting the images recorded with opposite probe helicities $P_{\pm 1, -1}(E_{\text{kin}}, \theta', t) - P_{\pm 1, +1}(E_{\text{kin}}, \theta', t)$, which results in

$$A^{\pm 1}(E_{\text{kin}}, \theta', t) = 2B_1(E_{\text{kin}}, t) P_1(\cos \theta') + 2B_3(E_{\text{kin}}, t) P_3(\cos \theta'). \quad (5)$$

Here again, in order to reduce the experimental uncertainties, the antisymmetric part of the raw images is first artificially symmetrized along the vertical axis contained in the polarization plane (which coincides with the pump polarization direction when $S_3 = 0$) and antisymmetrized along the light propagation axis (see Fig. 3(b)).

The set of $B_{\ell}(E_{\text{kin}}, t)$ coefficients are extracted from the symmetric and antisymmetric parts of the experimental images by using the relations (4) and (5). In practice, the symmetric and antisymmetric parts of the experimental images are fitted using the Legendre Polynomial projection basis $\{P_{\ell}(\cos \theta')\}$ with $\ell = 0 \dots 4$. The extracted B_{ℓ} are then divided by $\sqrt{2\ell + 1}$ in order to get the $B_{\ell, 2m=0}$. Using eqn (1), it is then possible to retrieve the 3D photoelectron distribution associated to the experimental projections.

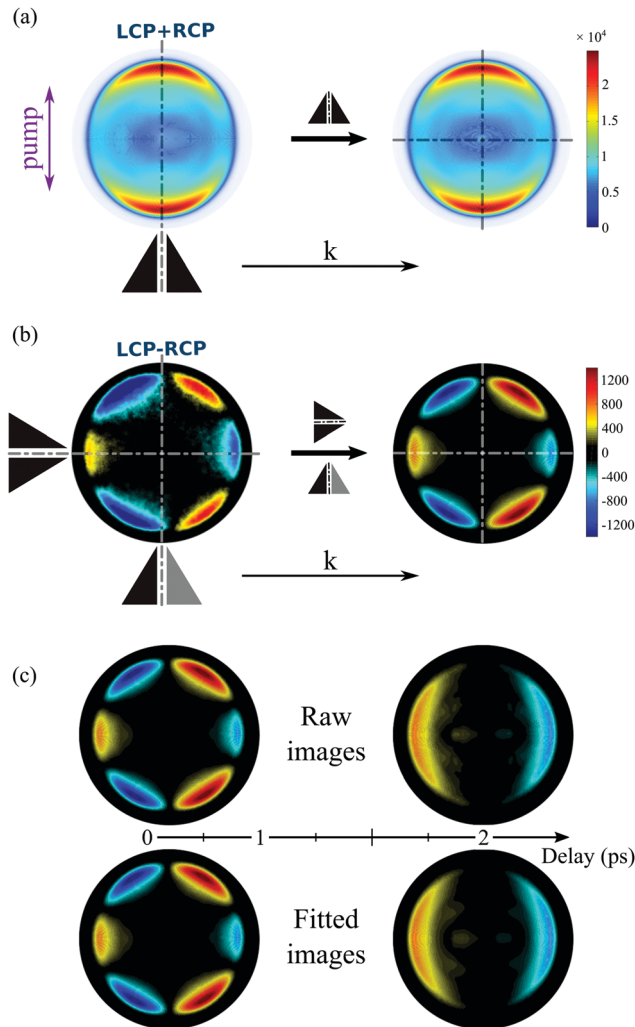


Fig. 3 (a) PECD being a normalized quantity, we need to measure the total number of electrons produced for each kinetic energy. This is achieved by the treatment of the symmetric part of the image – $S^{S_3}(E_{\text{kin}}, \theta', t)$ – shown here for the 100 fs delay and $S_3 = 0$. (b) The antisymmetric part of raw images – $A^{S_3}(E_{\text{kin}}, \theta', t)$ – is post-processed with first a symmetrization relative to the vertical direction contained in the polarization plane (similar to the pump polarisation when $S_3 = 0$), followed by an asymmetric operation relative to the propagation axis as illustrated for the same 100 fs pump–probe delay and $S_3 = 0$. The same contrast sensitivity is used for the raw and the processed images. (c) Fit of the antisymmetric images recorded in 1R,4R-(+)-camphor with a linearly polarized pump ($S_3 = 0$) that shows the quality of the fitting procedure of the images for two different delays despite the $2m = 0$ restricted decomposition.

In the present experiment, the ionization yields a single photoelectron peak located at a well fixed kinetic energy such that it is easy to define an angle- and energy-integrated TR-PECD, characterizing the degree of asymmetry of the whole ionization peak, as²³

$$\text{PECD}(t) = \frac{2\langle B_1 \rangle(t) - 0.5\langle B_3 \rangle(t)}{\langle B_0 \rangle(t)} = 2b_1(t) - 0.5b_3(t) \quad (6)$$

with $\langle B_{\ell} \rangle(t) = \int B_{\ell}(E_{\text{kin}}, t) dE_{\text{kin}}$, an integration performed over 130 meV centred at $E_{\text{kin}} = 0.5$ eV. Note that the difference

between the multiplicative factors appearing in front of the coefficient $B_3(E_{\text{kin}}, t)$ in eqn (5) and $\langle B_3 \rangle(t)$ in eqn (6) comes from the integration over the spherical angles that allows to pass from the projected representation of the asymmetry to its angularly integrated form.

2.2.2 TR-PECD with a linearly polarized pump. For a pump whose polarization state is \hat{x} , corresponding to a Stokes parameter $S_3 = 0$, the 3D photoelectron momentum distribution does not fulfill cylindrical symmetry anymore. The VMI-projected image in the (\hat{x}, \hat{z}) -plane is then

$$P_{0,\pm 1}(E_{\text{kin}}, \theta', t) = \sum_{\ell=0}^4 \sum_{\substack{m=-1 \\ |2m| \leq \ell}}^1 \mathcal{B}_{\ell,2m}^{0,\pm 1}(E_{\text{kin}}, t) P_{\ell}^{2m}(\cos \theta') \quad (7)$$

where $P_{\ell}^{2m}(\cos \theta')$ are projections of the real spherical harmonics introduced in (1). In practice, some of the $P_{\ell}^{2m}(\cos \theta')$ projections are linearly dependent, which prevents obtaining a unique set of $\mathcal{B}_{\ell,2m}^{0,\pm 1}(E_{\text{kin}}, t)$ parameters for a given t . We circumvent this issue by restricting the decomposition (7) to $2m = 0$, yielding

$$P_{0,\pm 1}(E_{\text{kin}}, \theta', t) = \sum_{\ell=0}^4 \tilde{\mathcal{B}}_{\ell}^{0,\pm 1}(E_{\text{kin}}, t) P_{\ell}(\cos \theta') \quad (8)$$

where tilde notations are employed to emphasize that this decomposition is biased with respect to the genuine physical symmetry of the interaction. Similarly to what has been done for TR-PECD with a circularly polarized pump, we use the following convention: $\tilde{B}_{\ell}(E_{\text{kin}}, t) = \tilde{B}_{\ell}^{0,-1}(E_{\text{kin}}, t)$, with $\tilde{B}_{\ell}^{0,+1}(E_{\text{kin}}, t) = (-1)^{\ell} \tilde{B}_{\ell}^{0,-1}(E_{\text{kin}}, t)$.

The symmetric and antisymmetric parts of the VMI images are obtained as in the case of a circularly polarized pump (see eqn (4) and (5)),

$$S^0(E_{\text{kin}}, \theta', t) = \tilde{B}_0(E_{\text{kin}}, t) P_0(\cos \theta') + \tilde{B}_2(E_{\text{kin}}, t) P_2(\cos \theta') + \tilde{B}_4(E_{\text{kin}}, t) P_4(\cos \theta'), \quad (9)$$

$$A^0(E_{\text{kin}}, \theta', t) = 2\tilde{B}_1(E_{\text{kin}}, t) P_1(\cos \theta') + 2\tilde{B}_3(E_{\text{kin}}, t) P_3(\cos \theta'). \quad (10)$$

We illustrate in Fig. 3(c) the accuracy of the reconstruction of the VMI signals in terms of the $2m = 0$ -restricted decomposition. The experimental $A^0(E_{\text{kin}}, \theta', t)$ antisymmetries are nicely reproduced by the fits (using eqn (10)) for $t = 100$ fs and $t = 2$ ps. The same accuracy is fulfilled for the symmetric parts $S^0(E_{\text{kin}}, \theta', t)$ of the distributions. The latter are not shown for the sake of conciseness. Contrary to the case where the excitation was induced by a circular polarization, when cylindrical symmetry is not maintained, *i.e.* for a linearly polarized pump, there is no *a priori* direct correspondence between the 3D electron distribution (1) involving $\mathcal{B}_{\ell,2m}^{0,\pm 1}$ coefficients and the experimental projections.

The integrated TR-PECD is defined similarly as before,

$$\widetilde{\text{PECD}}(t) = \frac{2\langle \tilde{B}_1 \rangle(t) - 0.5\langle \tilde{B}_3 \rangle(t)}{\langle \tilde{B}_0 \rangle(t)} = 2\tilde{b}_1(t) - 0.5\tilde{b}_3(t). \quad (11)$$

$\widetilde{\text{PECD}}(t)$ and $\tilde{b}_{1,3}(t)$ are the quantitative antisymmetric observables, normalized to the total number of photoelectrons. As established in ref. 23, while $\tilde{b}_1(t)$ describes the first-order asymmetric response, $\tilde{b}_3(t)$ describes the anisotropy of the asymmetric signal, induced by the pump excitation process.

Additionally to the comparisons made in Fig. 3(c), the reliability of the $2m = 0$ -restricted decomposition (eqn (8)) of the collected signals can be checked at the level of the integrated TR-PECD by comparing the result of eqn (11) with the direct experimental value, to which we refer to as 'raw' PECD. The latter is obtained as

$$\begin{aligned} \text{PECD}_{\text{raw}}(t) &= 4 \frac{\int_{-\pi/2}^{\pi/2} \int (P_{0,-1}(E_{\text{kin}}, \theta', t) - P_{0,+1}(E_{\text{kin}}, \theta', t)) dE_{\text{kin}} d\theta'}{\int_{-\pi/2}^{\pi/2} \int (P_{0,-1}(E_{\text{kin}}, \theta', t) + P_{0,+1}(E_{\text{kin}}, \theta', t)) dE_{\text{kin}} d\theta'}. \end{aligned} \quad (12)$$

3 Experimental results

We show in Fig. 4 the asymmetric part $A^0(E_{\text{kin}}, \theta', t)$ of the projected photoelectron momentum distributions obtained in (+)-camphor and (–)-fenchone for $S_3 = 0$ and prototypical pump–probe delays $t = 0.1, 1$ and 2 ps. These asymmetries are nothing else than unnormalized versions of the projected two-dimensional PECDs. Note that the normalized versions will be shown for other typical delays in Fig. 5(a).

At first glance, Fig. 4 is enough to observe qualitatively large isomeric effects between camphor and fenchone. First, at short delay, the 2D PECD of camphor exhibits a 6-lobe angular

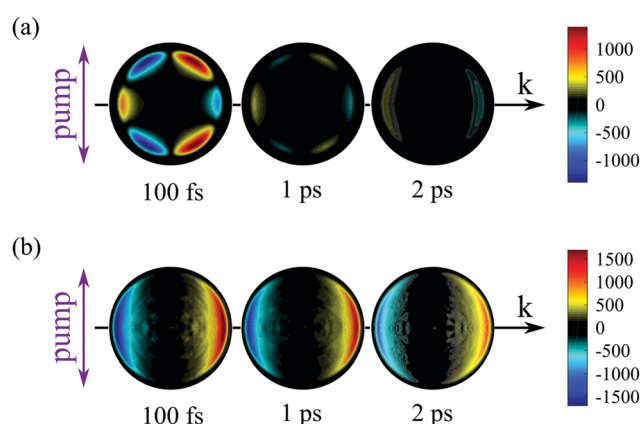


Fig. 4 The photoelectron images recorded on (a) 1R,4R-(+)-camphor and (b) 1R,4S-(–)-fenchone for each probe helicity, left-circularly polarized (LCP) and right-circularly polarized probe (RCP), are subtracted one from the other (LCP–RCP) and then processed as explained in Fig. 3 to get the photoelectron forward-backward asymmetric $A^0(E_{\text{kin}}, \theta', t)$ images relative to the propagation axis \vec{k} of the laser pulses. Here $S_3(\text{pump}) = 0$. These $A^0(E_{\text{kin}}, \theta', t)$ images plotted with the same contrast sensitivity show a drastic change as a function of the pump–probe delay: a forward asymmetry of the photoelectron before 1 ps converging to a backward one at longer delays in camphor (a), while fenchone maintains a forward asymmetry whatever the delay (b).

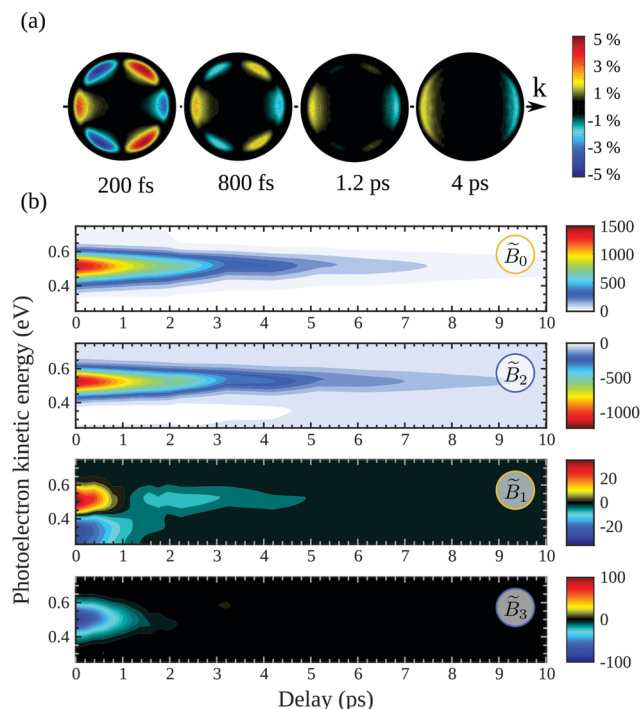


Fig. 5 TR-PECD in 1R,4R-(+)-camphor with $S_3(\text{pump}) = 0$: (a) for each delay t , the previous $A^0(E_{\text{kin}}, \theta', t)$ images are now normalized to the maximum of the corresponding $S^0(E_{\text{kin}}, \theta', t)$ images; (b) time and energy dependencies of the factors $\tilde{B}_0(E_{\text{kin}}, t)$, $\tilde{B}_2(E_{\text{kin}}, t)$, $\tilde{B}_1(E_{\text{kin}}, t)$ and $\tilde{B}_3(E_{\text{kin}}, t)$.

structure while its counterpart in fenchone has a fixed sign within the whole forward and backward hemispheres. Second, the angular structure of the PECD is maintained in both isomers between $t = 100$ fs and $t = 1$ ps, but the maximal amplitude of the 2D PECD decays faster in camphor than in fenchone. Third, the angular structure of the 2D PECD is lost between $t = 1$ and $t = 2$ ps in camphor while it hardly changes in fenchone within the same time interval. Finally, the overall preferential direction of electron ejection, defined as the integrated signal in the backward and forward hemisphere, is reversed between $t = 100$ fs and $t = 2$ ps in camphor, while electrons are preferentially emitted in the forward direction at all times in fenchone.

In order to perform a quantitative analysis of the ongoing dynamics, we now employ eqn (9) and (10) to extract from the symmetric $S^0(E_{\text{kin}}, \theta', t)$ and antisymmetric $A^0(E_{\text{kin}}, \theta', t)$ parts of the VMI signals the $\tilde{B}_i(E_{\text{kin}}, t)$ coefficients underlying the time-dependent photoelectron distribution in camphor. The same procedure was employed and illustrated in ref. 23 for fenchone. These coefficients are shown in Fig. 5(b). All the coefficients peak about a photoelectron kinetic energy $E_{\text{kin}} = 0.5$ eV in agreement with the previous (2 + 1)REMPI.^{14,15} This value is 0.1 eV lower than the one expected from vertical ionization from the 3s Rydberg intermediate state fulfilling the $\Delta E_{\text{vib}} = 0$ propensity rule. No salient feature depending on the electron kinetic energy shows up in Fig. 5(b). Indeed, our probe photon energy does not allow one to probe the rising population in the valence states originated from Rydberg-valence vibronic

relaxation since these states lie too low on the energy scale. The TR-PES, $\tilde{B}_0(E_{\text{kin}}, t)$, thus illustrates the monotonous decrease of the 3s-state population. $\tilde{B}_2(E_{\text{kin}}, t)$ corresponds to the anisotropy of symmetric differential electron ejection and remains significant as long as the 3s state is significantly populated, *i.e.* up to $t \sim 7$ ps. The higher-order anisotropy $\tilde{B}_4(E_{\text{kin}}, t)$, resulting from two-photon ionization, is very small (with a maximum of amplitude less than 1/7 of $\tilde{B}_2(E_{\text{kin}}, t)$) throughout the interaction. Accordingly, it is not displayed in Fig. 5(b). The analysis of the time-resolved symmetric photoelectron signal does not finally provide further information than the (expected) relaxation of the intermediate 3s state. Our previous study on TR-PECD in fenchone²³ led to the same conclusion.

We thus turn to the time-resolved antisymmetric part of VMI signals and the associated $\tilde{B}_1(E_{\text{kin}}, t)$ and $\tilde{B}_3(E_{\text{kin}}, t)$ Legendre coefficients. In fenchone,²³ we found that $\tilde{B}_3(E_{\text{kin}}, t) < \tilde{B}_1(E_{\text{kin}}, t)$ for all pump-probe delays t , which explains the shape of the 2D PECD that looks like the Legendre polynomial $P_1(\cos(\theta'))$ (see Fig. 4(b)). Moreover, the asymmetry, mainly dictated by $\tilde{B}_1(E_{\text{kin}}, t)$ in that case, was found to stay forward for all pump-probe delays. In contrast, Fig. 5(b) shows that in camphor, the absolute value of $\tilde{B}_3(E_{\text{kin}}, t)$ is stronger than that of $\tilde{B}_1(E_{\text{kin}}, t)$ at short delays. The anisotropy of the asymmetry, rationalized by $\tilde{B}_3(E_{\text{kin}}, t)$, is thus important in camphor at small t , yielding the 6-lobe angular structure observed in the 2D PECD of Fig. 4(a) and 5(a). This strong anisotropy of $A^0(E_{\text{kin}}, \theta', t)$ observed at small delay is the first isomeric effect revealed by the TR-PECDs of fenchone and camphor, consistently with the raw data shown in Fig. 4.

The main other difference between the two isomers is the sign reversal of $\tilde{B}_1(E_{\text{kin}}, t)$ in camphor at long delay. This sign switch appears around 1.2 ps and is concomitant with $\tilde{B}_3(E_{\text{kin}}, t)$ converging to zero (see Fig. 5(b)). This results in a TR-PECD which rapidly loses its angular structure and reverses the preferential direction of the electron to become backward as previously observed in Fig. 4(a) and 5(a).

In order to quantitatively extract the characteristic time-scales of the dynamics, we now turn our attention to the time-dependencies of the photoelectron yield $\langle \tilde{B}_0 \rangle(t)$ and normalized asymmetric coefficients $\tilde{b}_1(t)$ and $\tilde{b}_3(t)$ entering the definition (11) of $\widetilde{\text{PECD}}(t)$. These transients, shown in Fig. 6(a), have mono-exponential time-dependencies that can be fitted as

$$f(t) = y_0 + A \times \exp(-t/\tau) \times \left[1 + \text{erf} \left(\frac{2\sqrt{\ln 2}}{\tau_{\text{cc}}} \left(t - \frac{\tau_{\text{cc}}^2}{8\tau \ln 2} \right) \right) \right] \quad (13)$$

where τ is the decay constant inherent to each observable and τ_{cc} is the cross-correlation time of the pump and probe pulses. τ_{cc} and $t = 0$ have been determined by fitting the cation signal collected at the output of the time-of-flight detector (shown in Fig. 6(b)), leading to $\tau_{\text{cc}} = (190 \pm 10)$ fs.

Table 1 summarizes all the decay times τ and the asymptotic values extracted from the time-transients, as well as their counterparts for fenchone.²³ In the case where the 3s-Rydberg state is populated through the interaction with a linearly polarized pump ($S_3 = 0$), the decay time measured for the parent cation is

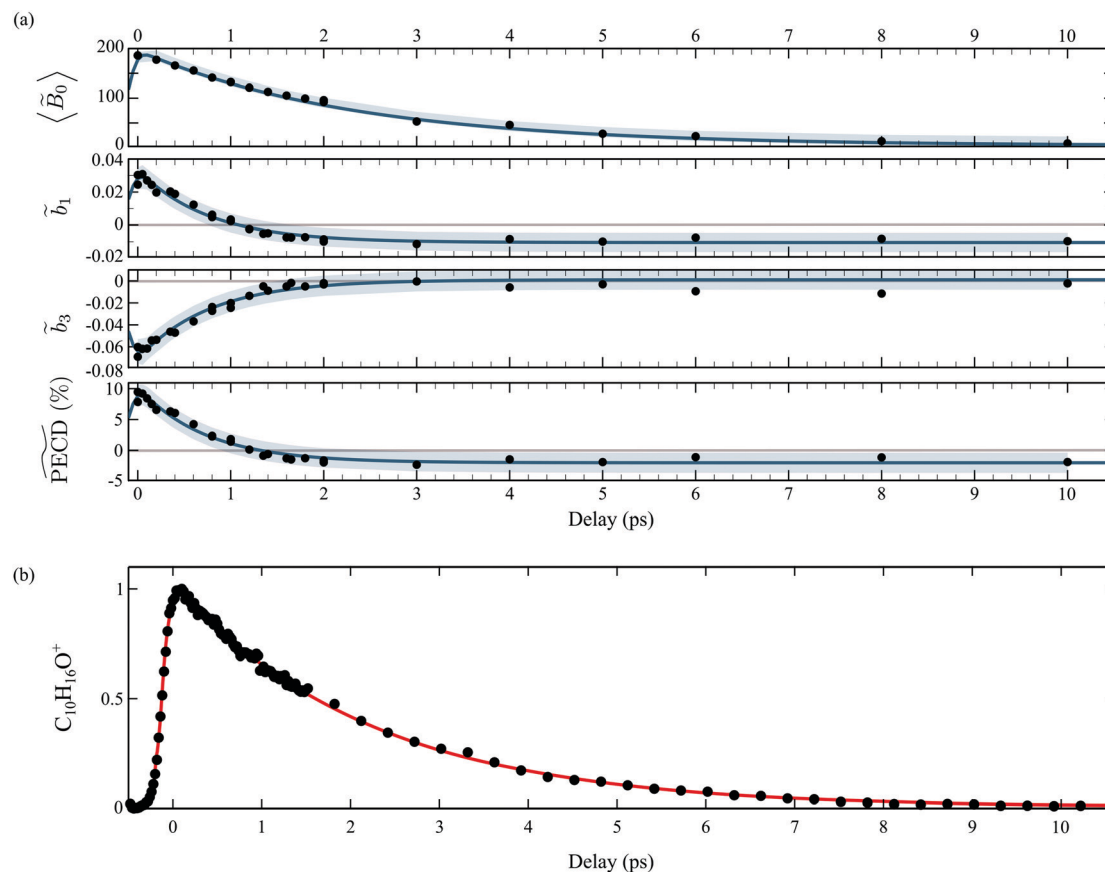


Fig. 6 (a) Time dependencies of the factors $\tilde{B}_0(E_{\text{kin}}, t)$, $\tilde{b}_1(t)$ and $\tilde{b}_3(t)$. The $\widetilde{\text{PECD}}$ percentage is then calculated by using eqn (11). The light blue areas correspond to the 50% confidence bounds of the fits using eqn (13). (b) Time-dependencies measured on the parent ion, which are normalised raw data without background subtraction on the contrary to the photoelectron images.

Table 1 Time constants extracted from the fits shown in Fig. 6 and 8 and for fenchone from ref. 23 with $S_3(\text{pump}) = 0$. The uncertainties correspond to 50% confidence bounds

Observables	1R,4R-(+)-Camphor – present work						1R,4S-(–)-Fenchone ²³	
	Decay (ps)			Converging value			Decay (ps)	Converging value
	$S_3 = 0$	$S_3 = -1$	$S_3 = 1$	$S_3 = 0$	$S_3 = -1$	$S_3 = 1$		
$C_{10}H_{16}O^+(t)$	2.20 ± 0.05						3.18 ± 0.04	
$\tilde{B}_0(t)$ or $B_0(t)$ (PES)	2.36 ± 0.07	2.65 ± 0.25	2.60 ± 0.29				3.28 ± 0.05	
$\tilde{b}_1(t)$ or $b_1(t)$	0.75 ± 0.05	2.07 ± 0.25	2.30 ± 0.18	−0.01	−0.02	−0.02	3.25 ± 0.5	0.073
$\tilde{b}_3(t)$ or $b_3(t)$	0.77 ± 0.04	1.28 ± 0.22	1.28 ± 0.20	0	0	0	1.4 ± 0.3	0
$\widetilde{\text{PECD}}(t)$ or $\text{PECD}(t)$	0.73 ± 0.05	1.94 ± 0.19	2.10 ± 0.14	−1.94%	−4.2%	−5%	3.25 ± 0.5	+14.6%
$\text{PECD}_r(t)$	0.84 ± 0.07	1.91 ± 0.40	2.05 ± 0.40	−1.36%	−3%	−3.6%		

$\tau(C_{10}H_{16}O^+) = 2.2$ ps while the photoelectron signal $\langle \tilde{B}_0 \rangle(t)$ decays within 2.36 ps. These decay times coincide, as expected for non-dissociative ionization, and characterize the timescale of vibronic relaxation of the 3s-Rydberg state into the valence states. As shown in Table 1, the 3s state relaxation is 25% slower in fenchone than in camphor. This is counterintuitive since the pump deposits more vibrational energy in the 3s state of fenchone than in camphor – 250 vs. 90 meV, according to the band origins of the 3s state in the respective isomers.^{15,20} Therefore, our results show that internal conversion is sensitive

to isomerism through the intricate and different vibrational dynamics taking place in the transient electronic state.

A larger, and totally unexpected, isomerism effect shows up in Table 1 as one compares the decay times of $\widetilde{\text{PECD}}$ in fenchone and camphor. In fenchone, $\tau(\widetilde{\text{PECD}}) \sim 3.3$ ps, which roughly corresponds to the 3s relaxation time. This means that the chiral asymmetry is encoded in the photoelectron yield almost as long as the intermediate 3s state is populated. The anisotropy of the asymmetry in fenchone, measured by \tilde{b}_3 , was found to decay faster ($\tau(\tilde{b}_3) = 1.4$ ps) as expected by the rotational dephasing of

the molecules due to a non-zero rotational temperature of fenchone.²³ But in camphor, PECD decays much faster than the 3s state relaxes: the time constants associated to $\langle \tilde{B}_0 \rangle$ and PECD are ~ 2.4 ps and ~ 0.7 ps, respectively. This means that the chiral photoelectron asymmetry has converged to a finite value long before the population of the transient 3s state, and subsequent ionization, vanish. This result could be artificial and due to the inadequacy of our analysis of the experimental images, based on the $2m = 0$ -restricted decomposition of the photoelectron signal – even if the reliability of this decomposition has been checked and presented in Fig. 3(c). Therefore, we directly evaluated the raw PECD according to eqn (12), and extracted both its decay time and asymptotic value. The agreement of raw and computed PECD, presented in Table 1, is reasonable and proves that the rapid loss of chiral asymmetry in $(1 + 1')$ -ionization of camphor is not artificially introduced by our $2m = 0$ -restriction. This faster decay could be rather due to fast internal vibrational relaxation (IVR), populating vibrational modes with inherent opposite PECDs and whose superposition leads to a vanishing net asymmetry.¹² In this respect, we observed such a fast IVR in fenchone:²³ the TR-PECD was found to decrease within ~ 400 fs before increasing smoothly on a ps timescale, towards its asymptotic value. We assigned this first 400 fs to a fast IVR, populating vibrational modes active in the internal conversion (IC) from 3s state to the valence ones but with opposite PECDs, while the subsequent ps increase of the net PECD was related to long-lived vibrational spectator modes of this same IC. In camphor, the TR-PECD continuously decreases from $t = 0$ onwards so that IVR and vibrationally selective internal conversion cannot be differentiated as easily as in fenchone. While the decrease of the PECD at small t can be safely ascribed to IVR, its subsequent evolution is monitored by both the vibrationally selective internal conversion and the loss of anisotropy of molecular orientations.

In order to gauge the influence of transient vibrational dynamics in the fast decay of PECD in camphor, we performed TR-PECD measurements with a circularly polarized pump ($S_3 = \pm 1$). Indeed, changing the pump polarisation state from $S_3 = 0$ to $S_3 = \pm 1$ does not modify the vibrational excitation, which means that any time dependencies related to IVR should be the same. Normalized $A^{+1}(E_{\text{kin}}, \theta', t)$ images, for a few delays, are presented in Fig. 7(a), while the associated temporal evolution of $B_{0-3}(E_{\text{kin}}, t)$ for $S_3 = \pm 1$, are displayed in Fig. 7(b) and (c). The decay constants of $B_{0-3}(E_{\text{kin}}, t)$ and PECD(t), as well as their asymptotic values, are listed in Table 1. Within the error bars, the dynamics recorded through both symmetric ($\langle B_0(t) \rangle$) and asymmetric ($b_{1,3}(t)$ and PECD(t)) observables do not depend on the helicity of the pump pulse. This is consistent with the fact that the 3s-state population, resulting from pump-induced sudden excitation, is identical for $S_3(\text{pump}) = 1$ and for $S_3(\text{pump}) = -1$. The time constant associated to 3s-state internal conversion is $\tau(B_0) = (2.6 \pm 0.25)$ ps for $S_3 = \pm 1$ while it is $\sim (2.36 \pm 0.07)$ ps for $S_3 = 0$: the 3s state relaxes within the same timescale whatever S_3 . However, while we observed that $\tau(b_1) \ll \tau(B_0)$ for $S_3 = 0$, we now recover the intuitive result $\tau(b_1) \sim \tau(B_0)$

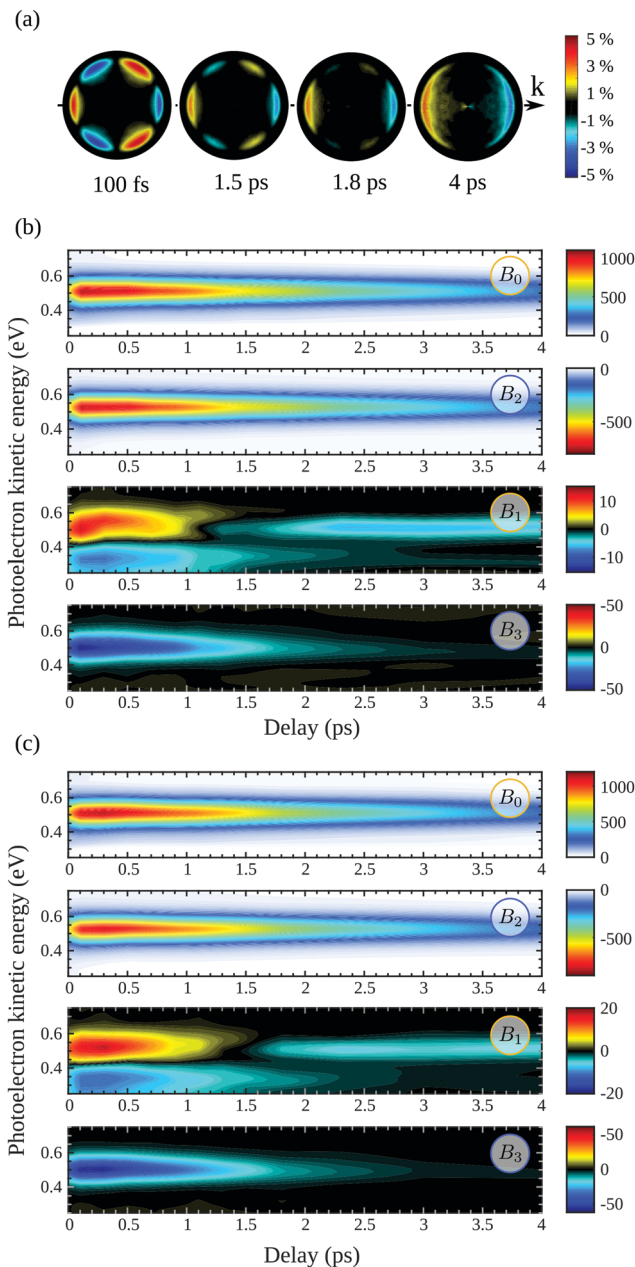


Fig. 7 TR-PECD in 1R,4R-(+)-camphor with $S_3(\text{pump}) = \pm 1$: (a) for each delay t , $A^{+1}(E_{\text{kin}}, \theta', t)$ images are now normalized to the maximum of the corresponding $S^{+1}(E_{\text{kin}}, \theta', t)$ images. Time and energy dependencies of the coefficients B_0 , B_2 , B_1 and B_3 extracted from the symmetric and anti-symmetric images recorded with a circularly polarized pump: (b) $S_3 = -1$ and (c) $S_3 = +1$.

observed in fenchone:²³ chirality survives throughout electron emission from the damped (relaxing) 3s state. We further observe that $\tau(b_3) < \tau(b_1)$ with $\tau(b_3) \sim 1.3$ ps. As in fenchone,²³ the latter timescale can be assigned once again to rotational dephasing since camphor has similar moments of inertia. We will come back to this loss of anisotropy of excitation further. Finally, the angle-integrated PECD, mainly monitored by b_1 , evolves with $\tau(\text{PECD}) \sim \tau(B_0)$. This comparison of $S_3(\text{pump}) = 0$ and ± 1 reveals a strong pump-polarization

angular PECD of fenchone and camphor at short delays. In the framework of $(1 + 1')$ -REMPI ionization, we consider non-overlapping pump and probe pulses of respective durations T_{pump} and T_{probe} and delayed by τ . Time t is referenced with respect to the time where the pump field maximizes. We restrict our description of the interaction to a (short) time range within which the nuclear structure of the molecules is assumed to remain frozen. Furthermore, we assume that the pump-induced excitation and the probe-induced ionization, both of which consist of absorption of one photon, are sudden processes which can be described within the Franck–Condon approximation. Vibrational dynamics can then be factored out from the transition amplitudes – they are described in terms of Franck–Condon factors which do not need to be taken into account explicitly when only relative quantities such as PECD are computed.³⁶

The photon absorption from low energy pulses can be fairly described by first-order perturbation theory. The pump pulse, with ellipticity S_3 , promotes the electron from the S_0 ground state to the 3s state whose population amplitude at time $t \geq T_{\text{pump}}/2$ is, for a molecular orientation $\hat{\mathbf{R}}$ in the laboratory frame:

$$a_{3s}^{S_3}(\hat{\mathbf{R}}, t) = i d_{S_0 \rightarrow 3s} \cdot \hat{\mathbf{e}}_{S_3}^{\text{mol}} E_{\text{pump}}(\omega) e^{-i\omega(t - T_{\text{pump}}/2)}. \quad (14)$$

$\omega = \varepsilon_{3s} - \varepsilon_{S_0}$ is the energy difference between the 3s and S_0 states, and $E_{\text{pump}}(\omega)$ is the spectral component of the pump pulse at frequency ω . $d_{S_0 \rightarrow 3s}$ is the transition dipole between the ground and the excited state in the molecular frame. This dipole, as well as the energies ε_{3s} and ε_{S_0} , has been computed using the GAMESS-US quantum chemistry package³⁷ using Time-Dependent Density Functional Theory (TDDFT).³⁸ The TDDFT calculations employed the CAM-B3LYP functional³⁹ and a 6-311++G** Gaussian basis⁴⁰ augmented with a set of diffuse Rydberg functions with symmetries (s,p,d,f) and exponents (0.045, 0.015, 0.005), located at the center of mass of the molecule. Note that the equilibrium geometry of the molecule was previously determined using DFT calculations with the B3LYP functional^{41,42} and the 6-311++G** basis. In eqn (14), $\hat{\mathbf{e}}_{S_3}^{\text{mol}}$ is the polarization unit vector of the pump, $\hat{\mathbf{e}}_{S_3}$, passively rotated into the molecular frame through $\hat{\mathbf{e}}_{S_3}^{\text{mol}} = \mathcal{R}(\hat{\mathbf{R}})\hat{\mathbf{e}}_{S_3}$, where $\mathcal{R}(\hat{\mathbf{R}})$ is a rotation matrix acting on the usual Euler angles (α, β, γ) which defines the molecular orientation $\hat{\mathbf{R}}$ in the laboratory frame.⁴³

A probe photon is subsequently absorbed and ionizes the molecule from the 3s excited state. The population amplitude of a continuum state defined by a wavevector \mathbf{k}_{mol} in the molecular frame is then, for $t \geq \tau + T_{\text{probe}}/2$:

$$a_{S_3, \pm 1}(\hat{\mathbf{R}}, \mathbf{k}_{\text{mol}}, t) = i a_{3s}^{S_3}(\hat{\mathbf{R}}, \tau - T_{\text{probe}}/2) \times d_{\mathbf{k}_{\text{mol}}} \cdot \hat{\mathbf{e}}_{\pm 1}^{\text{mol}} E_{\text{probe}}(\omega') e^{-i\omega'(t - \tau - T_{\text{probe}}/2)}. \quad (15)$$

The 3s state population amplitude enters the expression of the ionization amplitude as the initial condition of the ionization process. Similarly as before, $\hat{\mathbf{e}}_{\pm 1}^{\text{mol}}$ is the polarization unit vector of the circularly polarized probe pulse, passively rotated in the

molecular frame, and $E_{\text{probe}}(\omega')$ is the spectral component of the probe pulse, with $\omega' = IE + \varepsilon_{\mathbf{k}_{\text{mol}}} - \varepsilon_{3s} = IE + k_{\text{mol}}^2/2 - \varepsilon_{3s}$. $d_{\mathbf{k}_{\text{mol}}}$ is the ionization dipole linking the excited state Ψ_{3s} to the ingoing continuum state $\Psi_{\mathbf{k}_{\text{mol}}}^{(-)}$ and $d_{\mathbf{k}_{\text{mol}}} = \langle \Psi_{\mathbf{k}_{\text{mol}}}^{(-)} | \mathbf{r} | \Psi_{3s} \rangle$. The differential ionization cross section is directly proportional to the square modulus of the ionization amplitude. It is then clear from eqn (14) and (15) that this cross section does not depend on the time delay t . Then, in a $(1 + 1')$ -REMPI scheme involving only one intermediate state, the ionization cross section is stationary within the assumptions we made: Franck–Condon approximation and related frozen nuclear geometry for electronic transitions. Therefore, the expression of the ionization amplitude can be simplified by omitting all time-dependent factors, yielding

$$a_{S_3, \pm 1}(\hat{\mathbf{R}}, \mathbf{k}_{\text{mol}}) = a_{3s}^{S_3}(\hat{\mathbf{R}}, t = T_{\text{pump}}/2) d_{\mathbf{k}_{\text{mol}}} \cdot \hat{\mathbf{e}}_{\pm 1}^{\text{mol}} \quad (16)$$

which does not include the unimportant spectral components of the probe pulse. The calculation of the ionization dipole $d_{\mathbf{k}_{\text{mol}}}$ involves a partial-wave expansion of the ingoing scattering state:⁴⁴

$$\Psi_{\mathbf{k}_{\text{mol}}}^{(-)}(\mathbf{r}) = \sum_{l,m} i^l e^{-i\sigma_l} \Psi_{\mathbf{k}_{\text{mol}}lm}^{(-)}(\mathbf{r}) Y_l^{m*}(\theta_{\text{mol}}, \varphi_{\text{mol}}) \quad (17)$$

where σ_l is the Coulomb phase shift for wavevector \mathbf{k}_{mol} and angular momentum l , and $(\theta_{\text{mol}}, \varphi_{\text{mol}})$ points to the spherical direction of electron ejection in the molecular frame. $\Psi_{\mathbf{k}_{\text{mol}}lm}^{(-)}(\mathbf{r})$ are spherical complex states, fulfilling ingoing boundary conditions. Consistent with the partial-wave decomposition (17) of $\Psi_{\mathbf{k}_{\text{mol}}}^{(-)}$ into spherical harmonics, the rotation of the unit polarization vector $\hat{\mathbf{e}}_{\pm 1}$ in the molecular frame is expressed in the spherical basis $\{\hat{\mathbf{e}}_{\nu}\}_{\nu=-1,0,1}$ where the rotation matrix \mathcal{R} reduces to its Wigner \mathcal{D} -form,⁴⁵ e.g. $\hat{\mathbf{e}}_{\pm 1}^{\text{mol}} = \sum_{\nu} \mathcal{D}_{\nu, \pm 1}^{(1)} \hat{\mathbf{e}}_{\nu}$. Inserting (17) into (16), one thus obtains

$$a_{S_3, \pm 1}(\hat{\mathbf{R}}, \mathbf{k}_{\text{mol}}) = a_{3s}^{S_3}(\hat{\mathbf{R}}, t = T_{\text{pump}}/2) \times \sum_{lm\nu} (-i)^l e^{i\sigma_l} \mathcal{D}_{\nu, \pm 1}^{(1)}(\hat{\mathbf{R}}) a_{\mathbf{k}_{\text{mol}}lm\nu} Y_l^{m*}(\theta_{\text{mol}}, \varphi_{\text{mol}}) \quad (18)$$

where $a_{\mathbf{k}_{\text{mol}}lm\nu} = \langle \Psi_{\mathbf{k}_{\text{mol}}lm}^{(-)} | \mathbf{r} \cdot \hat{\mathbf{e}}_{\nu} | \Psi_{3s} \rangle$ are the partial-wave ionization amplitudes.

For a given molecular orientation, the cross section in the molecular frame is then

$$\begin{aligned} \sigma_{S_3, \pm 1}^{\text{mol}}(\hat{\mathbf{R}}, \mathbf{k}_{\text{mol}}) &\propto \left| a_{S_3, \pm 1}(\hat{\mathbf{R}}, \mathbf{k}_{\text{mol}}) \right|^2 \\ &= P_{3s}^{S_3}(\hat{\mathbf{R}}, t = T_{\text{pump}}/2) \\ &\times \left| \sum_{lm\nu} (-i)^l e^{i\sigma_l} \mathcal{D}_{\nu, \pm 1}^{(1)}(\hat{\mathbf{R}}) a_{\mathbf{k}_{\text{mol}}lm\nu} Y_l^{m*}(\theta_{\text{mol}}, \varphi_{\text{mol}}) \right|^2. \end{aligned} \quad (19)$$

where $P_{3s}^{S_3}(\hat{\mathbf{R}}, t = T_{\text{pump}}/2)$ is the population of the 3s state at the end of the pump pulse whose ellipticity is defined by the

Stokes parameter S_3 . In the lab frame, the electron ejection is defined by $\mathbf{k} = (k, \theta, \varphi)$ with $k = k_{\text{mol}}$. We thus apply a rotation from the molecular to the lab frame to obtain the differential cross section in the latter:

$$\begin{aligned} \sigma_{S_3, \pm 1}(\hat{\mathbf{R}}, \mathbf{k}) &= P_{3s}^{S_3}(\hat{\mathbf{R}}, t = T_{\text{pump}}/2) \\ &\times \left| \sum_{lm\nu} (-i)^l e^{i\sigma_l} \mathcal{D}_{\nu, \pm 1}^{(1)}(\hat{\mathbf{R}}) a_{klm\nu} \right. \\ &\times \left. \sum_{\mu} \mathcal{D}_{m, \mu}^{l*}(\hat{\mathbf{R}}) Y_l^{\mu}(\theta, \varphi) \right|^2 \end{aligned} \quad (20)$$

The target sample consists of a set of randomly oriented molecules. The average cross section associated to the whole sample is thus

$$\mathcal{P}_{S_3, \pm 1}(E_{\text{kin}}, \theta, \varphi) = \frac{1}{8\pi^2} \int \sigma_{S_3, \pm 1}(\hat{\mathbf{R}}, \mathbf{k}) d\hat{\mathbf{R}} \quad (21)$$

where $E_{\text{kin}} = k^2/2$. Using algebra inherent to spherical harmonics and Wigner rotation matrices,⁴⁵ similar to the one employed *e.g.* in ref. 32, one can further show that the differential cross section (20) can be put into the form of eqn (1). In practice, the orientation averaging (21) has been performed using a numerical quadrature based on \mathcal{N} -uniformly distributed orientations $\hat{\mathbf{R}}_i = (\alpha_i, \beta_i, \gamma_i)$, with $i = 1, \dots, \mathcal{N}$, and Euler angular spacing $\Delta\alpha = \Delta\beta = \Delta\gamma = \pi/24$. Then,

$$\mathcal{P}_{S_3, \pm 1}(E_{\text{kin}}, \theta, \varphi) = \sum_i w_i \sigma_{S_3, \pm 1}(\hat{\mathbf{R}}_i, \mathbf{k}) \quad (22)$$

where w_i are the integration weights.

Once the 3D cross section has been computed, we simulate the 2D distributions collected on the VMI plane by integrating $\mathcal{P}_{S_3, \pm 1}(E_{\text{kin}}, \theta, \varphi)$ along the TOF-dimension y perpendicular to the detector plane:

$$P_{S_3, \pm 1}(E_{\text{kin}}, \theta') = \int \mathcal{P}_{S_3, \pm 1}(E_{\text{kin}}, \theta, \varphi) dp_y \quad (23)$$

where θ' is the polar angle in the VMI plane, used in the definitions (2) and (8) of VMI images. The angularly resolved 2D PECD is then defined as

$$\text{PECD}_{2D}(E_{\text{kin}}, \theta') = 2 \frac{P_{S_3, -1}(E_{\text{kin}}, \theta') - P_{S_3, +1}(E_{\text{kin}}, \theta')}{P_{\text{max}}} \quad (24)$$

where P_{max} is the maximum value of $P_{S_3, -1}(E_{\text{kin}}, \theta') + P_{S_3, +1}(E_{\text{kin}}, \theta')$ along θ' for a given kinetic electron energy E_{kin} . Using eqn (1), only enantio-selective terms appear in the expression of the 2D PECD:

$$\begin{aligned} \text{PECD}_{2D}(E_{\text{kin}}, \theta') &= \frac{4}{P_{\text{max}}} [\mathcal{B}_{1,0}(E_{\text{kin}}, \theta') P_1^0(\theta') \\ &+ \mathcal{B}_{2,-2}(E_{\text{kin}}, \theta') P_2^{-2}(\theta') \\ &+ \mathcal{B}_{3,0}(E_{\text{kin}}, \theta') P_3^0(\theta') \\ &+ \mathcal{B}_{3,2}(E_{\text{kin}}, \theta') P_3^2(\theta') \\ &+ \mathcal{B}_{4,-2}(E_{\text{kin}}, \theta') P_4^{-2}(\theta')] \end{aligned} \quad (25)$$

where $P_\ell^{2m}(\theta')$ are projections of the real spherical harmonics $Y_\ell^{2m}(\theta, \varphi)$ onto the VMI detector plane (see eqn (7)) and $\mathcal{B}_{l,2m} \equiv \mathcal{B}_{l,2m}^{S_3, -1}$ to shorten the notation. The total, angularly integrated, PECD is defined as

$$\begin{aligned} \text{PECD}(E_{\text{kin}}) &= 4 \frac{\int_{-\pi/2}^{\pi/2} d\theta' (P_{S_3, -1}(E_{\text{kin}}, \theta') - P_{S_3, +1}(E_{\text{kin}}, \theta'))}{\int_{-\pi/2}^{\pi/2} d\theta' (P_{S_3, -1}(E_{\text{kin}}, \theta') + P_{S_3, +1}(E_{\text{kin}}, \theta'))} \\ &= \frac{2\sqrt{3}\mathcal{B}_{1,0}(E_{\text{kin}}) - \frac{\sqrt{7}}{2}\mathcal{B}_{3,0}(E_{\text{kin}})}{\mathcal{B}_{0,0}(E_{\text{kin}})} \end{aligned} \quad (26)$$

which can be written as

$$\text{PECD}(E_{\text{kin}}) = 2b_1(E_{\text{kin}}) - \frac{b_3(E_{\text{kin}})}{2} \quad (27)$$

where $b_1(E_{\text{kin}}) = \sqrt{3}\mathcal{B}_{1,0}(E_{\text{kin}})/\mathcal{B}_{0,0}(E_{\text{kin}})$ and $b_3(E_{\text{kin}}) = \sqrt{7}\mathcal{B}_{3,0}(E_{\text{kin}})/\mathcal{B}_{0,0}(E_{\text{kin}})$. Note that all coefficients $\mathcal{B}_{l,2m}$ with $2m \neq 0$ vanish in the expression of the angularly integrated PECD since $\int_{-\pi/2}^{\pi/2} d\theta' P_l^{2m}(\cos \theta') \equiv \int_0^{2\pi} d\varphi \int_0^{\pi/2} d\theta \sin(\theta) Y_\ell^{2m}(\theta, \varphi) = 0$ for $2m \neq 0$.

Calculations have been run for (+)-camphor and (−)-fenchone, considering that (1 + 1')-REMPI yields in both cases a photoelectron signal centred about $E_{\text{kin}} = 0.5$ eV, as in the experiments. In practice, the spherical ingoing states $\Psi_{k_{\text{mol}}lm}^{(-)}(\mathbf{r})$, involved in the computation of $a_{k_{\text{mol}}lm\nu}$, are decomposed into real states $\psi_{k_{\text{mol}}lm}(\mathbf{r})$ which are obtained by diagonalizing the coupled-channel (multi-scattering) Schrödinger equation $H_0 \psi_{k_{\text{mol}}lm}(\mathbf{r}) = \frac{k_{\text{mol}}^2}{2} \psi_{k_{\text{mol}}lm}(\mathbf{r})$. H_0 is the unperturbed Hamiltonian. In the TDDFT framework, the excited state Ψ_{3s} only results from one-electron excitations from the HOMO to virtual orbitals. Therefore, we assume that the ionic core also remains frozen during the transition from 3s to the continuum. Accordingly, H_0 is an effective one-electron Hamiltonian which can be decomposed as $H_0 = -\frac{1}{2}\nabla^2 + V$ where V is the effective potential of the ionic core on the ejected electron. We employ an approximate description of this potential, in terms of the so-called ElectroStatic Potential (ESP) charges⁴⁶ which basically consist of non-integer charges Z_i^{eff} located on the nuclei of the molecule. The effective charges are determined to fit the genuine potential on van der Waals surfaces surrounding the atoms in the molecule according to

$$V(\mathbf{r}) = - \sum_i \frac{Z_i}{|\mathbf{r} - \mathbf{R}_i|} + \int \frac{\rho(\mathbf{r}')}{|\mathbf{r} - \mathbf{r}'|} d\mathbf{r}' \sim - \sum_i \frac{Z_i^{\text{eff}}}{|\mathbf{r} - \mathbf{R}_i|} \quad (28)$$

Z_i and \mathbf{R}_i are the real charges and locations of the nuclei while $\rho(\mathbf{r})$ is the ionic electron density.

The computed 2D PECD with $S_3(\text{pump}) = 0$ is shown in Fig. 9(a) and (b), respectively. The angular structure of the 2D PECD associated to camphor is in excellent agreement with its experimental counterpart, displayed in Fig. 4(a). Six lobes of alternating sign are appearing along the photoelectron ring, which illustrates the importance of anisotropic effects in the

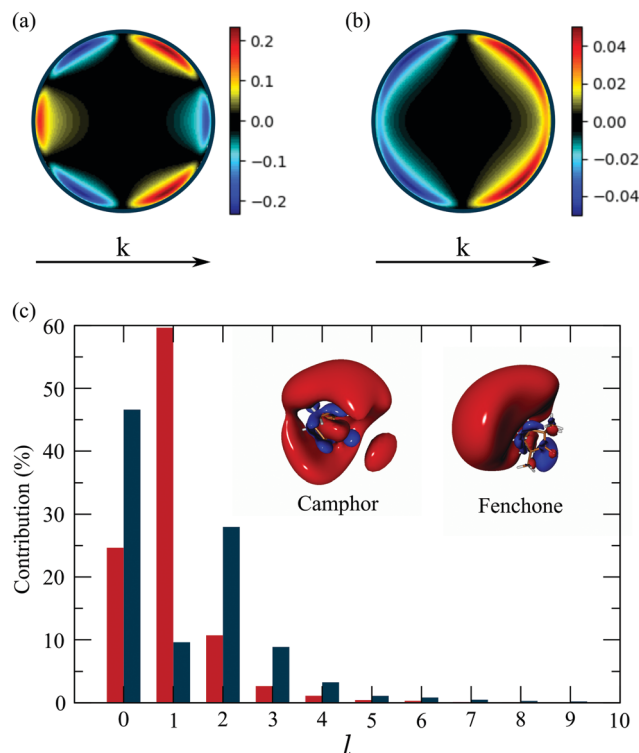


Fig. 9 Theoretical angular PECD at $t = 0$ in (a) camphor and (b) fenchone. (c) Decomposition of 3s-Rydberg state orbitals for camphor (blue) and fenchone (red) as a function of l number at $t = 0$.

chiral asymmetric part of the 3D differential cross section. These effects are quantified by the ratio \tilde{b}_3/\tilde{b}_1 which is equal to -2 (see Table 2). The excellent agreement found in camphor slightly deteriorates for fenchone. Even if the computed 2D PECD (shown in Fig. 9(b)) exhibits a positive sign in the whole forward hemisphere, as in the experiment displayed in Fig. 4(b), the computed PECD distribution is angularly more structured. In fenchone, at the opposite of camphor, the anisotropic part of chiral asymmetry (b_3) is thus considerably weaker than its isotropic part (b_1) in both calculations and experiments, but the isotropic/anisotropic relative sign is reversed. Indeed while $b_3/b_1 = -0.45$ in the calculations, $\tilde{b}_3/\tilde{b}_1 = +0.44$ in the experiments. The computed values of the angularly integrated PECDs shown in Fig. 9 are $+5.7\%$ and $+5.6\%$ in (+)-camphor and (–)-fenchone, respectively. They are in reasonable agreement with the measurements that yield $+9\%$ and $+10\%$ for the two respective isomers. In the following, we rely on this experimental/theoretical agreement of 2D PECDs to track the origin of the isomeric effect observed between fenchone and camphor.

The 3D photoelectron angular distribution depends on three factors: (i) the anisotropy of the molecular spatial distribution induced by the polarization of the pump in the primary excitation process, (ii) the shape of the excited state orbital as the initial condition of the ionization process, and (iii) the structure of the chiral continuum reached during ionization. As outlined above, the chiral continuum is described in terms of ESP charges which are obviously different in fenchone and camphor. However, we

ran some simulations where the continuum was described in terms of hydrogenic wavefunctions in both isomers. These simulations have yielded 2D PECDs in qualitative agreement with those of Fig. 9(a) and (b), still exhibiting very different angular shapes in both isomers. This indicates that the structure of the continuum (iii) is not primarily responsible for the isomeric effect. In our simulations, both camphor and fenchone molecules are oriented such that the $3s \leftarrow S_0$ excitation dipole lies along the \hat{z}^{mol} direction in the molecular frame. The pump, linearly polarized along \hat{x} in the laboratory frame, thus leads to the same effective conical alignment about \hat{x} , so that (i) can be ruled out as the single source of the isomeric effect. However, the dynamical alignment also determines the preferential orientation of the intermediate $3s$ state as the initial condition of the ionization process. The influence of the shape of the excited state orbital, whose orientation in the lab frame is determined at the end of excitation, should thus mainly explain the isomerism effect. In this respect, the isomeric effect observed in usual one-photon XUV ionization experiments⁷ is explained in terms of isomer-dependent scattering of the escaping electron in the chiral potential. Here this effect is strongly lowered since ionization occurs from a Rydberg orbital whose diffuseness limits interaction with the core chirality.

The excited state is directly involved in the definition of the partial-wave ionization amplitudes $a_{k_{\text{mol}}lm\nu} = \langle \Psi_{k_{\text{mol}}lm}^{(-)} | \mathbf{r} \cdot \hat{\mathbf{e}}_{\nu} | \Psi_{3s} \rangle$. These amplitudes are calculated employing a partial-wave expansion of the excited state:

$$\Psi_{3s}(\mathbf{r}) = \sum_{lm} \Psi_{lm}(r) Y_l^m(\theta, \varphi). \quad (29)$$

The larger are the l -angular momenta involved in this decomposition, the larger are the l' momenta populated in the continuum through $a_{k_{\text{mol}}l'm'\nu}$ because of the usual dipolar selection rules inherent to the $\mathbf{r} \cdot \hat{\mathbf{e}}_{\nu}$ operator. The angular momentum l' in the continuum controls the amplitude of the $\mathcal{B}_{\ell,m}^{S_3,\pm 1}$ coefficients determining the differential cross section (2) since $|l' - l''| \leq \ell \leq l' + l''$, where l' and l'' are here both continuum momenta. Therefore, an excited state whose partial-wave decomposition mainly consists of one l -contribution will lead to a small $\mathcal{B}_{3,0}^{S_3,\pm 1}$ coefficient while extended l -excited states are amenable to large anisotropy coefficients. We estimate the l -contribution to the (normalized) $3s$ excited state as

$$C_l = \sum_m \int_0^\infty |\Psi_{lm}(r)|^2 dr. \quad (30)$$

The C_l contributions are displayed in Fig. 9(c) for fenchone and camphor. We observe that the l -distribution extends to larger l in camphor than in fenchone, which basically explains the larger $\mathcal{B}_{3,0}^{S_3,\pm 1}$ coefficient and related exacerbated anisotropy in the former isomer. We thus answer the first question raised in Section 3: in our $(1 + 1')$ -REMPI scheme, isomeric effects at short delays are mainly due to the shape of the intermediate excited state.

4.2 TR-PECD and rotational dephasing at long delays

We now turn our attention to the time evolution of PECD in camphor, with the aim to understand the mechanisms responsible for the difference in the PECD decay observed for $S_3 = 0$ and $S_3 = \pm 1$. We also aim at understanding why the PECD switches sign around $t \sim 1$ –2 ps.

Taking into account the ps timescale involved here, we drew from our description of PECD at short delays in the S_0 equilibrium geometry and introduced in our model rotational dephasing effects coupled to the effective alignment created by the pump within the randomly oriented sample. Rotational dephasing consists in describing the temporal evolution of the molecular orientation, $\hat{\mathbf{R}}(t)$, consistent with the temperature of the molecular sample. Here, rotational dephasing is described classically, as in ref. 47 and 48. At the end of the pump pulse, the molecular orientation $\hat{\mathbf{R}}(T_{\text{pump}}/2) = (\alpha(T_{\text{pump}}/2), \beta(T_{\text{pump}}/2), \gamma(T_{\text{pump}}/2))$ is converted to the quaternion representation $\{q_i\}$, with $i = 1, \dots, 4$.⁴³ Rotational dynamics is then completely described in the representation in terms of the seven differential equations:

$$\begin{pmatrix} \frac{dq_1}{dt} \\ \frac{dq_2}{dt} \\ \frac{dq_3}{dt} \\ \frac{dq_4}{dt} \end{pmatrix} = \frac{1}{2} \begin{pmatrix} q_4 & q_3 & -q_2 & -q_1 \\ -q_3 & q_4 & q_1 & -q_2 \\ q_2 & -q_1 & q_4 & -q_3 \\ q_1 & q_2 & q_3 & q_4 \end{pmatrix}^{-1} \begin{pmatrix} \Omega_x \\ \Omega_y \\ \Omega_z \\ 0 \end{pmatrix} \quad (31)$$

$$\begin{pmatrix} \frac{d\Omega_x}{dt} \\ \frac{d\Omega_y}{dt} \\ \frac{d\Omega_z}{dt} \end{pmatrix} = \begin{pmatrix} \frac{I_{yy} - I_{zz}}{I_{xx}} \Omega_y \Omega_z \\ \frac{I_{zz} - I_{xx}}{I_{yy}} \Omega_z \Omega_x \\ \frac{I_{xx} - I_{yy}}{I_{zz}} \Omega_x \Omega_y \end{pmatrix}$$

where Ω_i , with $i = x, y, z$, are the angular velocities along the principal axis i of the molecule. The initial molecular distribution is represented by \mathcal{N} (with $\mathcal{N} = 51 \times 51 \times 25$) orientations weighted by the transition amplitude $a_{3s}^{S_3}(\hat{\mathbf{R}}, t = T_{\text{pump}}/2)$ (see eqn (14)). For each weighted trajectory, several hundred velocities Ω_i ($N_v = 500$) are chosen randomly to form a normal distribution centered around $\Omega_i = \sqrt{\frac{k_B T}{I_{ii}}}$, where T is the rotational temperature and I_{ii} is the moment of inertia associated to the principal axis i . In camphor, $I_{x,y,z} = 1241, 1521$ and 1639 amu Bohr² for the S_0 ground state equilibrium geometry. The set of $\tilde{\mathcal{N}} = \mathcal{N} \times N_v$ weighted trajectories is propagated according to eqn (31) until $t = 5$ ps. At a given delay t , the $\tilde{\mathcal{N}}$ molecular orientations are extracted and quaternions are converted back to Euler angles $\hat{\mathbf{R}}_j(t) = (\alpha_j(t), \beta_j(t), \gamma_j(t))$ with

$j = 1, \dots, \tilde{\mathcal{N}}$. Ionization then occurs, and the differential cross section, averaged on the $\tilde{\mathcal{N}}$ orientations, is defined as

$$\mathcal{P}_{S_3, \pm 1}(E_{\text{kin}}, \theta, \varphi) = \frac{1}{\tilde{\mathcal{N}}} \sum_{j=1}^{\tilde{\mathcal{N}}} w_j \sigma_{S_3, \pm 1}(\hat{\mathbf{R}}_j(t), \mathbf{k}) \quad (32)$$

where w_j , the integration weights, are identical for all the velocities associated to a given initial orientation. The orientation-dependent ionization cross section is adapted from eqn (20):

$$\begin{aligned} \sigma_{S_3, \pm 1}(\hat{\mathbf{R}}_j(t), \mathbf{k}) &= P_{3s}^{S_3}(\hat{\mathbf{R}}_j(T_{\text{pump}}/2), t = T_{\text{pump}}/2) \\ &\times \left| \sum_{lm\nu} (-i)^l e^{i\sigma_l} \mathcal{D}_{\nu, \pm 1}^{(1)}(\hat{\mathbf{R}}_j(t)) a_{klm\nu} \right. \\ &\times \left. \sum_{\mu} \mathcal{D}_{m, \mu}^{l*}(\hat{\mathbf{R}}_j(t)) Y_l^{\mu}(\theta, \varphi) \right|^2. \end{aligned} \quad (33)$$

Importantly, we still do not account for vibrational dynamics – the molecules remain frozen at their S_0 equilibrium geometry. In order to reduce the computational cost, the rotational temperature has been set to 100 K in our simulations, which overestimates the experimental one (~ 10 –30 K). However, as shown in previous studies,⁴⁹ this is not problematic and provides an appropriate illustration of the impact of the rotational dephasing on the PECD. In summary, at lower rotational temperature T , all the features described below will occur but with longer time constants.

The temporal evolution of the 2D PECD is shown in Fig. 10(a) for $S_3(\text{pump}) = 0$. We observe that the angular structure of the PECD, linked to a strong negative $B_{3,0}$, changes drastically at $t \sim 1.5$ ps and vanishes for $t > 3$ ps. Asymptotically, all but $B_{1,0}^{S_3, \pm 1}$ coefficients are zero in the expression of the differential cross section. This is fully consistent with the fact that at 3 ps, the distribution of molecular orientations is uniform. Therefore ionization occurs from a randomly oriented 3s-state, yielding a PECD shape similar to the well-known one-photon ionisation (VUV-PECD restricted to b_1). Fig. 10(a) also includes the simulated images for $S_3 = \pm 1$. We observe then that the loss of PECD angular structuring decreases faster in that case, with the 6-lobe patterns hardly visible for $t \gtrsim 1$ ps. In conclusion, the effective molecular alignment does not impact identically a PECD undergoing a rotational dephasing. However, this sensitivity vanishes as time elapses beyond ~ 3 ps resulting in 2D-PECD images almost identical for $S_3 = 0$ and $S_3 = \pm 1$.

We present in Fig. 10(c) the angularly integrated TR-PECD of these images for $S_3 = 0$ (line) and $S_3 = \pm 1$ (dots). The PECD reverses sign about $t \sim 1$ ps. This is quite consistent with our experiments where such a sign switch has been also observed (see Table 2). However, while the magnitude of the computed PECDs is in reasonable agreement with the experiments at $t = 0$, the calculations overestimate it at long delays ($\sim -7.5\%$ vs. $\sim -2\%$). An immediate explanation for such a discrepancy could be that our model neglects some dynamics such as the ongoing vibrational relaxation converging to the 3s-state equilibrium geometry. To partially take into account such geometry

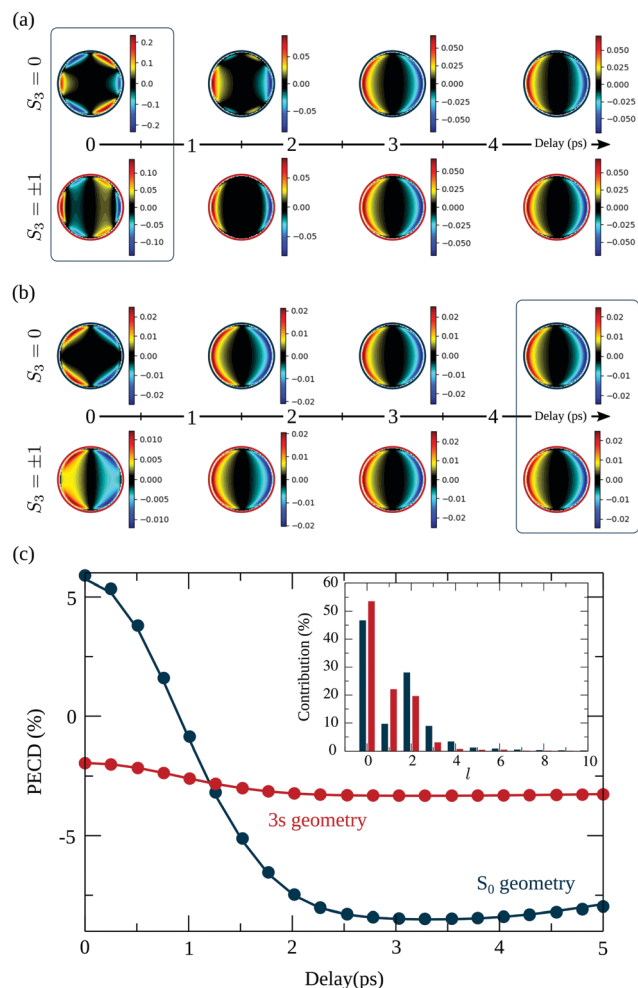


Fig. 10 Theoretical study of the influence of rotational dephasing in camphor on (a) the 2D-PECD calculated in the S_0 ground state geometry for different pump polarization and as a function of the pump–probe delay. (b) Same calculations but in the equilibrium geometry of the $3s$ Rydberg state. (c) Evolution of angularly integrated TR-PECD, in percent, as a function of the delay for linear (line) and circular (dots) pump polarization for molecules in the S_0 ground state equilibrium geometry (blue) and molecules in the $3s$ Rydberg state geometry (red). In the inset is given the $3s$ -Rydberg orbital l -decomposition for the S_0 ground state equilibrium geometry (blue) and $3s$ equilibrium geometry (red).

change, we implemented calculations where the ionization amplitudes and the moment of inertia were computed at the $3s$ -state equilibrium geometry. The results are shown in Fig. 10(b) and (c). Despite the little changes between the S_0 and $3s$ equilibrium geometries – less than 3% of internuclear distances – the shape of the $3s$ state is significantly altered between these two nuclear configurations. This has a drastic impact on the 2D PECDs visible by comparing Fig. 10(a) and (b) at $t = 0$, for both $S_3 = 0$ and $S_3 = \pm 1$. For instance, in the $3s$ geometry, the photoelectron asymmetries are backward whatever the delay. We also note that the loss of PECD angular structuring takes place on a shorter timescale compared to S_0 geometry: the final (b_1) shape is reached as soon as $t \sim 1.5$ ps. In conclusion, not only the effective molecular alignment induced by the pump but also the shape of the intermediate state is equally

important for the subsequent temporal evolution of the PECD. We show in the inset of Fig. 10 that the l -distributions of the $3s$ state are indeed quite different in S_0 and $3s$ equilibrium geometries. This explains, according to the conclusion of the previous section, the distinct magnitudes and shapes of the PECDs associated to the different nuclear geometries. Asymptotically, the angularly integrated PECD computed in the $3s$ equilibrium geometry (shown in Fig. 10(c)) is $\sim -3\%$, which is closer to our experimental asymptotic values. Merging S_0 results at short delays and $3s$ ones at long times could then provide a temporal evolution of the TR-PECD qualitatively compatible with our experimental measurements displayed in Fig. 8.

However, a major shortcoming of our model appears in Fig. 10(c): in contrast to what the experiments have shown in Fig. 8, our simulations yield an angularly integrated PECD which does not depend on the polarization of the pump (within numerical deviations due to the finite number of molecular orientations). In practice, the computations indicate that the b_1 and b_3 coefficients, which define the angularly integrated PECD according to eqn (27), do not depend on S_3 (pump). This last statement might seem counter-intuitive since the angular patterns of the 2D-PECD images shown in Fig. 10(a) and (b) depend clearly on S_3 (pump). The explanation is quite simple: these images include contributions of projected spherical harmonics $P_l^{2m}(\cos \theta')$, with $2m \neq 0$, which depend on S_3 but vanish as one performs the angular integration of the 2D PECD to get its angularly integrated form (see eqn (25)–(29)). This explains why 2D-PECD images might depend on S_3 while their integration leads to the same net asymmetry. We explicitly checked from a formal point of view that this is expected within the framework of our model which employs the Franck-Condon approximation to model $(1 + 1')$ -ionization involving a single intermediate state.

On the other hand, our model does not include nuclear dynamics which could lead to the experimentally observed S_3 -dependence of the angularly integrated PECD. Let's introduce the basic equations associated to these dynamics subsequent to the excitation process. We consider Born–Oppenheimer molecular states $\Psi_{i,j}(\mathbf{r}, \mathbf{R}) = \phi_i(\mathbf{r}, \mathbf{R})\chi_{i,j}(\mathbf{R})$ where $\phi_i(\mathbf{r}, \mathbf{R})$ are electronic eigenfunctions and $\chi_{i,j}(\mathbf{R})$ are vibrational states within the i th electronic surface. First-order transitions from the ground ($i = 0, j = 0$) to the vibrationally excited ($i = 3s, j$) states lead to the formation of a time-dependent vibrational wavepacket, after the pump ends:

$$\psi_{3s}(\mathbf{R}, t) = \sum_j c_{3s,j} \chi_{3s,j}(\mathbf{R}) e^{-i\varepsilon_{3s,j}(t - T_{\text{pump}}/2)} \quad (34)$$

where $\varepsilon_{i,j}$ are the total (electronic + vibrational) energies associated to $\Psi_{i,j}(\mathbf{r}, \mathbf{R})$. In the Franck–Condon approximation, the amplitudes $c_{3s,j}$ are

$$c_{3s,j} = -iE_{\text{pump}}(\omega_j) \int d\mathbf{r} \phi_{3s}^*(\mathbf{r}, \mathbf{R}_0) \mathbf{r} \cdot \hat{\mathbf{e}}_{S_3}^{\text{mol}} \phi_0(\mathbf{r}, \mathbf{R}_0) \times \int d\mathbf{R} \chi_{3s,j}(\mathbf{R}) \chi_{0,0}(\mathbf{R}) \quad (35)$$

where $E_{\text{pump}}(\omega_j = \varepsilon_{3s,j} - \varepsilon_{0,0})$ and $\hat{e}_{S_3}^{\text{mol}}$ are defined as in eqn (14) and the electronic dipole $\int d\mathbf{r} \phi_{3s}^*(\mathbf{r}, \mathbf{R}) \mathbf{r} \cdot \hat{e}_{S_3}^{\text{mol}} \phi_0(\mathbf{r}, \mathbf{R})$ is evaluated at the equilibrium geometry \mathbf{R}_0 of the molecule in its ground state. This dipolar term thus consists of a global factor which can be also factored out in the expression (34) of the vibrational wavepacket. In other words, nuclear dynamics do not depend on S_3 in the Franck–Condon approximation. However, our Franck–Condon simulations do show that the 2D-PECD, projected onto the VMI plane, depends on S_3 . This has to be related to the effective alignment (selection of molecular orientations according to $\mathbf{r} \cdot \hat{e}_{S_3}^{\text{mol}}$) operated by the pump during the excitation process. This anisotropy disappears at the level of angularly integrated PECD, as the usual b_2 -anisotropy remains hidden in measurements of total cross sections.

Importantly, beyond the Franck–Condon approximation, the amplitudes $c_{3s,j}$ read

$$c_{3s,j} = -iE_{\text{pump}}(\omega_j) \times \int d\mathbf{R} \chi_{3s,j}(\mathbf{R}) \chi_{0,0}(\mathbf{R}) \times \int d\mathbf{r} \phi_{3s}^*(\mathbf{r}, \mathbf{R}) \mathbf{r} \cdot \hat{e}_{S_3}^{\text{mol}} \phi_0(\mathbf{r}, \mathbf{R}) \quad (36)$$

where $\langle \phi_{3s} | \mathbf{r} \cdot \hat{e}_{S_3}^{\text{mol}} | \phi_0 \rangle_r$ is a function of \mathbf{R} that depends on S_3 ; e.g., $\langle \phi_{3s} | \mathbf{r} \cdot \hat{e}_{S_3=0}^{\text{mol}} | \phi_0 \rangle_r(\mathbf{R}) \neq \langle \phi_{3s} | \mathbf{r} \cdot \hat{e}_{S_3=1}^{\text{mol}} | \phi_0 \rangle_r(\mathbf{R})$. The electronic dipolar term can no longer be factored out, so that both the amplitude and phase of the vibrational wavepacket, *i.e.* the nuclear dynamics, now explicitly depend on the polarization state S_3 of the pump. As a matter of fact, we have mimicked non-Franck–Condon transitions by introducing two non-collinear dipoles in our calculations. This amounts to a discretized version of $c_{3s,j}$ in eqn (36) where $\int d\mathbf{R} \rightarrow \sum_{\mathbf{R}_1, \mathbf{R}_2}$. Even if

we did not include explicitly the vibrational wavefunctions, this allowed us to represent the population of different regions of the 3s surface landscape, beyond the Franck–Condon assumption. In practice, the first dipole has been set to $\sqrt{0.7} \mathbf{d}_{S_0 \rightarrow 3s}$ while the second one was $\sqrt{0.3} \mathbf{d}_{S_0 \rightarrow 3s}$ rotated in a direction perpendicular to the first one. The subsequent description of ionization has been made using S_0 and 3s nuclear geometries for \mathbf{R}_1 and \mathbf{R}_2 , respectively. We then obtained different angularly integrated PECDs for $S_3 = 0$ (+8.58%) and $S_3 = \pm 1$ (+4.87%), similarly to our experimental observations. On the basis of these last simulations and previous discussions, we conclude that non-Franck–Condon transitions are at play in the experiments. Such non-Franck–Condon transitions have already been observed in standard VUV-PECD of methyloxirane,¹² and in PhotoExcitation Circular Dichroism (PXCD)⁵⁰ involving a single intermediate electronic state in camphor. Similar transitions could be also at play in fenchone, but due to the weak b_3 , their fingerprint is not as visible as in camphor.

It has to be noted that as soon as the intermediate excited state is reached through absorption of $n > 1$ photons, the angularly integrated PECD does depend on the polarization

state S_3 of the pump in the Franck–Condon framework. This can be already understood in a simple two-photon excitation scheme where the absorption cross section, averaged over the molecular orientations, already depends on S_3 .⁵¹ This is highly beneficial to simulations of multiphoton PECD using either linearly or circularly polarized pump photons³² since the vibrational dynamics, which can be factored out from the ionization amplitude, does not need to be explicitly taken into account.

In its present form, our model cannot explain in depth the PECD time-transients observed in the $(1 + 1')$ -ionization process. Since it employs the Franck–Condon approximation, it is reliable for short delays and at asymptotic times where ionization occurs as the molecules are in their S_0 and 3s equilibrium geometries, respectively (both regions are highlighted in Fig. 10(a) and (b)). However, the model allows one to understand how the rotational dephasing, coupled to the effective alignment induced by the pump and the shape of the intermediate state involved in the $(1 + 1')$ -ionization scheme, influences drastically the temporal evolution of the angularly resolved PECD and can also result in a switch of the PECD.

5 Conclusions

We have investigated the sensitivity of TR-PECD to isomerism effects using (–)-fenchone and (+)-camphor as prototypical molecules primarily excited in their 3s state.

At short delays, strong differences are observed in the angular PECD between the two isomers. In order to understand these differences, we have developed a theoretical model, based on first order perturbation theory, where the nuclear geometry of the molecules is frozen throughout the $(1 + 1')$ -photon absorption. We have thus been able to highlight the crucial role of the shape of the intermediate excited state in this isomerism effect.

At longer delay, using a linearly polarized pump, we found that while no isomeric-dependent features appear in the TR-PES, the TR-PECD is drastically different between the two isomers, in both its time transients and temporal evolution of the angular structure. We varied the pump polarization, going from $S_3 = 0$ to $S_3 = \pm 1$, in order to decorrelate the different degrees of freedom. Indeed, in the context of a Franck–Condon vertical transition, the vibrational excitation in the 3s state is expected to be the same in both cases, and only the spatial molecular anisotropy, due to excitation, differs. The measurements showed that the time constants associated with the chiral observables are very different for $S_3 = 0$ and $S_3 = \pm 1$ in camphor. The PECD decays much faster for $S_3 = 0$ than for $S_3 = \pm 1$, with its time dependence being in the latter case close to the behavior observed in fenchone. We extended our model to take into account the rotational dephasing of the molecular orientations after the excitation step. The temporal evolution of the 2D PECD showed that the rotational degree of freedom is coupled to the pump-induced molecular alignment and to the shape of the intermediate excited state. However, the model yields identical integrated PECDs for $S_3 = 0$ and $S_3 = \pm 1$, in contrast to the experiment. We traced back the root of this behaviour by the use of the Franck–Condon approximation.

Therefore, we inferred that the experiments reveal that non Franck–Condon transitions are at play in the $(1 + 1')$ -interaction scheme. The coupling of such vibrational dynamics to the external (rotational) degree of freedom is consistent with PECD time-transients depending on S_3 and isomeric effects between fenchone and camphor.

The influence of the loss of anisotropy of excitation observed here may have consequences for the high-resolution REMPI-PECD measurements, which aim at addressing as a resonant intermediate state a given vibrational level of the electronic excited state. Recent measurements have shown that using nanosecond pulses, the REMPI-PECD was rather insensitive to the intermediate vibrational levels.¹⁶ As illustrated in Fig. 10, using shorter pulses may enable keeping the benefit of the anisotropy of excitation and reveal the influence of vibrational excitation. A trade-off between spectral resolution and a laser interaction duration shorter than the loss of anisotropy could be obtained by using tunable Fourier-limited picosecond pulses.

The high sensitivity of TR-PECD to molecular alignment revealed by our study indicates that resolving the 3D distributions of the PECD would provide more spectroscopic information, through the evolution of the anisotropy of the chiral response. The continuous variation of the degree of ellipticity of the exciting radiation, in a multiphoton pump scheme, would allow manipulating the anisotropy of excitation and the resulting dichroism.²⁰ Furthermore, resolving the molecular alignment through coincidence electron ion imaging⁵² would enable drawing a complete picture of the relaxation dynamics, even if such a goal remains experimentally challenging in terms of acquisition time of the measurements.

Last, broadening the range of pump and probe photon energies would enable investigating other important processes, such as the vibrational relaxation subsequent to inner-shell electronic excitation and the photorelaxation of reactive excited states such as π^* states, or to track the chiral response around conical intersections. Such studies would make TR-PECD an observable of choice to answer fundamental questions in photochemistry.

Conflicts of interest

There are no conflicts to declare.

Acknowledgements

This project has received funding from the European Research Council (ERC) under the European Unions Horizon 2020 research and innovation program no. 682978 – EXCITERS, and 654148. We acknowledge the financial support of the French National Research Agency through ANR-14-CE32-0014 MISFITS and from the Région Nouvelle Aquitaine through RECHIRAM, as well as Université of Bordeaux.

Notes and references

- 1 B. Ritchie, *Phys. Rev. A: At., Mol., Opt. Phys.*, 1976, **13**, 1411–1415.
- 2 I. Powis, *J. Chem. Phys.*, 2000, **112**, 301–310.

- 3 N. Böwering, T. Lischke, B. Schmidtke, N. Müller, T. Khalil and U. Heinzmann, *Phys. Rev. Lett.*, 2001, **86**, 1187–1190.
- 4 L. Nahon, G. A. Garcia and I. Powis, *J. Electron Spectrosc. Relat. Phenom.*, 2015, **204**, 322–334.
- 5 S. Beaulieu, A. Comby, A. Clergerie, J. Caillat, D. Descamps, N. Dudovich, B. Fabre, R. Géneaux, F. Légaré, S. Petit, B. Pons, G. Porat, T. Ruchon, R. Taeb, V. Blanchet and Y. Mairesse, *Science*, 2017, **358**, 1288–1294.
- 6 H. Ganjitarbar, G. A. Garcia, L. Nahon and I. Powis, *J. Chem. Phys.*, 2020, **153**, 034302.
- 7 L. Nahon, L. Nag, G. Garcia, I. Myrgorodska, U. J. Meierhenrich, S. Beaulieu, V. Wanie, V. Blanchet, R. Géneaux and I. Powis, *Phys. Chem. Chem. Phys.*, 2016, **18**, 12696–12706.
- 8 S. Turchini, D. Catone, N. Zema, G. Contini, T. Prosperi, P. Decleva, M. Stener, F. Rondino, S. Piccirillo, K. C. Princ and M. Speranza, *ChemPhysChem*, 2013, **14**, 1723–1732.
- 9 S. Daly, M. Tia, G. A. Garcia, L. Nahon and I. Powis, *Angew. Chem., Int. Ed.*, 2016, **128**, 11220–11224.
- 10 T. Lischke, N. Böwering, B. Schmidtke, N. Müller, T. Khalil and U. Heinzmann, *Phys. Rev. A: At., Mol., Opt. Phys.*, 2004, **70**, 022507.
- 11 S. Daly, I. Powis, G. A. Garcia, H. Soldi-Lose and L. Nahon, *J. Chem. Phys.*, 2011, **134**, 064306.
- 12 G. A. Garcia, L. Nahon, S. Daly and I. Powis, *Nat. Commun.*, 2013, **4**, 2132.
- 13 M. M. RaffeeFanoood, H. Ganjitarbar, G. A. Garcia, L. Nahon, S. Turchini and I. Powis, *ChemPhysChem*, 2018, **19**, 921–933.
- 14 C. Lux, M. Wollenhaupt, T. Bolze, Q. Liang, J. Köhler, C. Sarpe and T. Baumert, *Angew. Chem., Int. Ed.*, 2012, **51**, 5001–5005.
- 15 C. S. Lehmann, N. B. Ram, I. Powis and M. H. M. Janssen, *J. Chem. Phys.*, 2013, **139**, 234307.
- 16 A. Kastner, G. Koumariannou, P. Glodic, P. C. Samartzis, N. Ladda, S. T. Ranecky, T. Ring, S. Vasudevan, C. Witte, H. Braun, H.-G. Lee, A. Senftleben, R. Berger, G. B. Park, T. Schäfer and T. Baumert, *Phys. Chem. Chem. Phys.*, 2020, **22**, 7404–7411.
- 17 S. Beaulieu, A. Ferré, R. Géneaux, R. Canonge, D. Descamps, B. Fabre, N. Fedorov, F. Légaré, S. Petit, T. Ruchon, V. Blanchet, Y. Mairesse and B. Pons, *New J. Phys.*, 2016, **18**, 102002.
- 18 E. Bloch, S. Larroque, S. Rozen, S. Beaulieu, A. Comby, S. Beauvarlet, D. Descamps, B. Fabre, S. Petit, R. Taeb, A. J. Uzan, V. Blanchet, N. Dudovich, B. Pons and Y. Mairesse, *Phys. Rev. X*, 2021, in press.
- 19 H. Ganjitarbar, R. Hadidi, G. A. Garcia, L. Nahon and I. Powis, *J. Mol. Spectrosc.*, 2018, **353**, 11–19.
- 20 A. Comby, E. Bloch, C. M. M. Bond, D. Descamps, J. Miles, S. Petit, S. Rozen, J. B. Greenwood, V. Blanchet and Y. Mairesse, *Nat. Commun.*, 2018, **9**, 5212.
- 21 M. M. R. Fanoood, N. B. Ram, C. S. Lehmann, I. Powis and M. H. M. Janssen, *Nat. Commun.*, 2015, **6**, 7511.
- 22 A. Kastner, C. Lux, T. Ring, S. Züllighoven, C. Sarpe, A. Senftleben and T. Baumert, *ChemPhysChem*, 2016, **17**, 1119–1122.
- 23 A. Comby, S. Beaulieu, M. Boggio-Pasqua, D. Descamps, F. Légaré, L. Nahon, S. Petit, B. Pons, B. Fabre, Y. Mairesse and V. Blanchet, *J. Phys. Chem. Lett.*, 2016, **7**, 4514–4519.

- 24 S. Beaulieu, A. Comby, B. Fabre, D. Descamps, A. Ferré, G. Garcia, R. Généaux, F. Légaré, L. Nahon, S. Petit, T. Ruchon, B. Pons, V. Blanchet and Y. Mairesse, *Faraday Discuss.*, 2016, 325–348.
- 25 L. Nahon, G. A. Garcia, H. Soldi-Lose, S. Daly and I. Powis, *Phys. Rev. A: At., Mol., Opt. Phys.*, 2010, **82**, 032514.
- 26 C. Lux, M. Wollenhaupt, C. Sarpe and T. Baumert, *Chem-PhysChem*, 2015, **16**, 115–137.
- 27 S. Beaulieu, A. Comby, D. Descamps, S. Petit, F. Légaré, B. Fabre, V. Blanchet and Y. Mairesse, *J. Chem. Phys.*, 2018, **149**, 134301.
- 28 N. Fedorov, S. Beaulieu, A. Belsky, V. Blanchet, R. Bouillaud, M. De Anda Villa, A. Filippov, C. Fourment, J. Gaudin, R. E. Grisenti, E. Lamour, A. Lévy, S. Macé, Y. Mairesse, P. Martin, P. Martinez, P. Noé, I. Papagiannouli, M. Patanen, S. Petit, D. Vernhet, K. Veyrinas and D. Descamps, *Rev. Sci. Instrum.*, 2020, **91**, 105104.
- 29 U. Even, I. Al-Hroub and J. Jortner, *J. Chem. Phys.*, 2001, **115**, 2069–2073.
- 30 M. Hillenkamp, S. Keinan and U. Even, *J. Chem. Phys.*, 2003, **118**, 8699–8705.
- 31 F. Pulm, J. Schramm, J. Hormes, S. Grimme and S. Peyerimhoff, *Chem. Phys.*, 1997, **224**, 143–155.
- 32 R. E. Goetz, T. A. Isaev, B. Nikoobakht, R. Berger and C. P. Koch, *J. Chem. Phys.*, 2017, **146**, 024306.
- 33 A. G. Harvey, Z. Mašín and O. Smirnova, *J. Chem. Phys.*, 2018, **149**, 064104.
- 34 G. A. Garcia, L. Nahon and I. Powis, *Rev. Sci. Instrum.*, 2004, **75**, 4989–4996.
- 35 A. Blokhin, M. Gelin, E. Khoroshilov, I. Kryukov and A. Sharkov, *Opt. Spectrosc.*, 2003, **95**, 346–352.
- 36 G. A. Garcia, L. Nahon, S. Daly and I. Powis, *Nat. Commun.*, 2013, **4**, 2132.
- 37 M. Schmidt, K. Baldrige, J. Boatz, S. Elbert, M. Gordon, J. Jenson, S. Koseki, N. Matsunaga, K. Nguyen, S. Su, T. Windus, M. Dupuis and J. Montgomery, *J. Comput. Chem.*, 1993, **14**, 1347–1363.
- 38 E. Runge and E. K. U. Gross, *Phys. Rev. Lett.*, 1984, **52**, 997–1000.
- 39 T. Yanai, D. P. Tew and N. C. Handy, *Chem. Phys. Lett.*, 2004, **393**, 51–57.
- 40 R. Krishnan, J. S. Binkley, R. Seeger and J. A. Pople, *J. Chem. Phys.*, 1980, **72**, 650–654.
- 41 A. D. Becke, *Phys. Rev. A: At., Mol., Opt. Phys.*, 1988, **38**, 3098–3100.
- 42 C. Lee, W. Yang and R. G. Parr, *Phys. Rev. B: Condens. Matter Mater. Phys.*, 1988, **37**, 785–789.
- 43 H. Goldstein, *Classical Mechanics*, Addison-Wesley, 1980.
- 44 D. Dill and J. L. Dehmer, *J. Chem. Phys.*, 1974, **61**, 692–699.
- 45 M. E. Rose and B. T. Feld, *Phys. Today*, 1957, **10**, 30.
- 46 B. H. Besler, K. M. Merz Jr. and P. A. Kollman, *J. Comput. Chem.*, 1990, **11**, 431–439.
- 47 D. C. Rapaport, *Rigid molecules*, Cambridge University Press, 2nd edn, 2004, pp. 199–244.
- 48 A. Kol, B. B. Laird and B. J. Leimkuhler, *J. Chem. Phys.*, 1997, **107**, 2580–2588.
- 49 D. Baykusheva, D. Zindel, V. Svoboda, E. Bommeli, M. Ochsner, A. Tehlar and H. J. Wörner, *Proc. Natl. Acad. Sci. U. S. A.*, 2019, **116**, 23923–23929.
- 50 S. Beaulieu, A. Comby, D. Descamps, B. Fabre, G. A. Garcia, R. Généaux, A. G. Harvey, F. Légaré, Z. Mašín, L. Nahon, A. F. Ordonez, S. Petit, B. Pons, Y. Mairesse, O. Smirnova and V. Blanchet, *Nat. Phys.*, 2018, **14**, 484–489.
- 51 F. Zahariev and M. S. Gordon, *J. Chem. Phys.*, 2014, **140**, 18A523.
- 52 M. Tia, M. Pitzer, G. Kastirke, J. Gatzke, H.-K. Kim, F. Trinter, J. Rist, A. Hartung, D. Trabert, J. Siebert, K. Henrichs, J. Becht, S. Zeller, H. Gassert, F. Wiegandt, R. Wallauer, A. Kuhlins, C. Schober, T. Bauer, N. Wechselberger, P. Burzynski, J. Neff, M. Weller, D. Metz, M. Kircher, M. Waitz, J. B. Williams, L. P. H. Schmidt, A. D. Müller, A. Knie, A. Hans, L. Ben Ltaief, A. Ehresmann, R. Berger, H. Fukuzawa, K. Ueda, H. Schmidt-Böcking, R. Dörner, T. Jahnke, P. V. Demekhin and M. Schöffler, *J. Phys. Chem. Lett.*, 2017, **8**, 2780–2786.